Master of Science Thesis

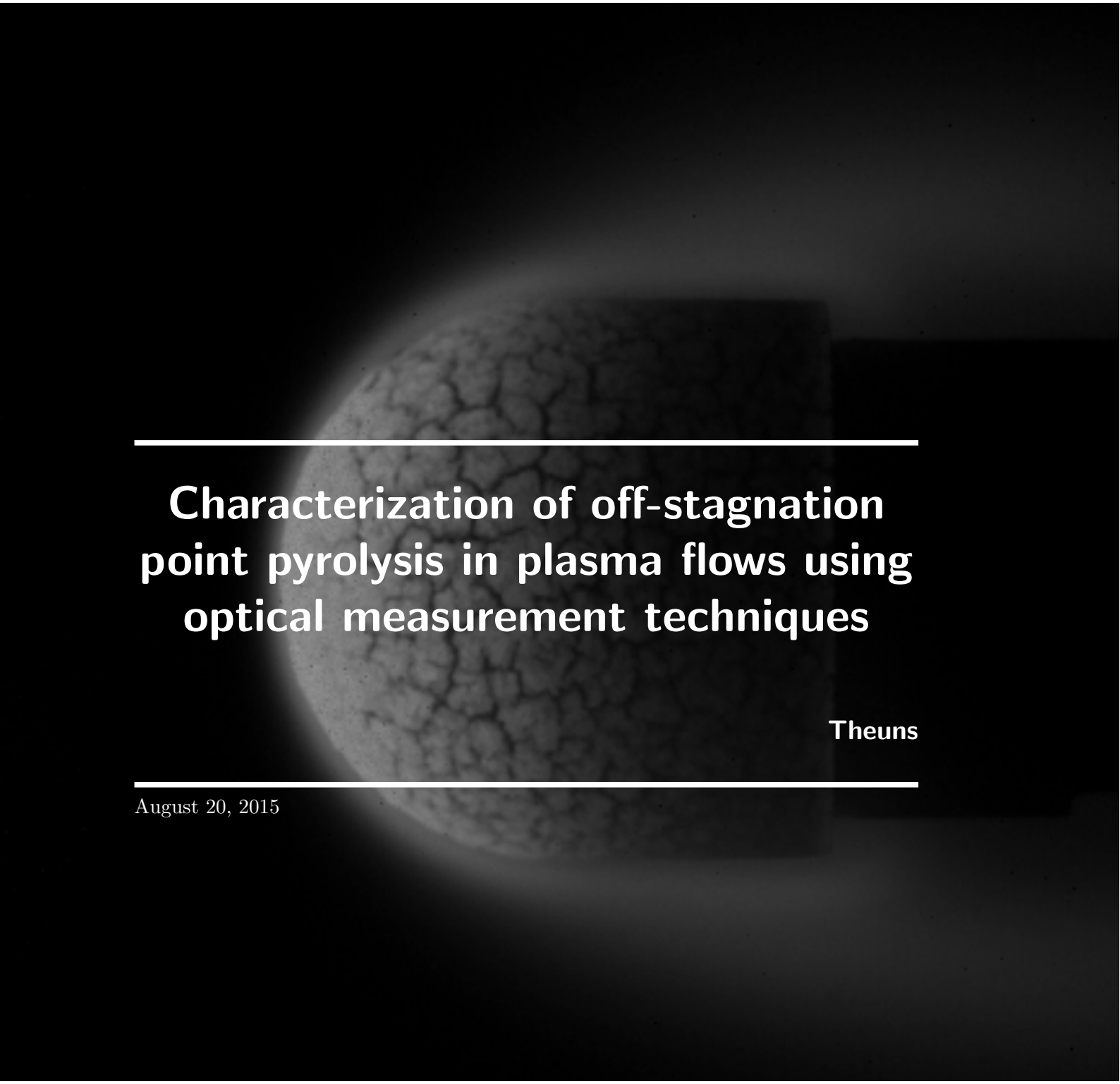

Characterization of off-stagnation point pyrolysis in plasma flows using optical measurement techniques

Theuns

August 20, 2015

Aerodynamics

TU Delft

Faculty of Aerospace Engineering

Delft University of Technology

Characterization of off-stagnation point pyrolysis in plasma flows using optical measurement techniques

Master of Science Thesis

For obtaining the degree of Master of Science in Aerospace Engineering at Delft University of Technology

Theuns

August 20, 2015

Faculty of Aerospace Engineering · Delft University of Technology

Delft University of Technology

DELFT UNIVERSITY OF TECHNOLOGY
DEPARTMENT OF AERODYNAMICS

The undersigned hereby certify that they have read and recommend to the Faculty of Aerospace Engineering for acceptance the thesis entitled **"Characterization of off-stagnation point pyrolysis in plasma flows using optical measurement techniques"** by **Theuns** in fulfillment of the requirements for the degree of **Master of Science**.

Dated: August 20, 2015

Supervisors:

Dr. ir. F.F.J. Schrijer

Dr. ir. B.W. van Oudheusden

Prof. Dr. Ing G. Eitelberg

Ir. B. Helber

Table of Contents

List of Figures

List of Tables

Chapter 1

Introduction

After the invention of the rocket mankind saw a new possibility to study the universe and other planets than Earth by space travel. Since then man has achieved to orbit Earth, land on the Moon and Mars. The constant increase in the demands of future space exploration mission make that also the equipment needs to be fit to the task. For example in 2020 NASA aims at returning a sample from Mars back to Earth [NASA Mars Exploration Program & Missions].

Due to the long distances and thus long duration of these missions, often it is chosen to employ the shortest transit trajectories. The transit time is the time it takes to change orbit, this together with the wait time in orbit gives the total travel duration. If one would travel to Mars using a Hohmann transfer it would take them more than 200 days while with a Parabolic transfer it would take less than 70 days. A schematic of the transfers is given in figure 1.1. Paired with this difference in transit time, goes the energy needed for these transfers. The Hohmann transfer is known to be energy efficient and thus the entry velocity will be low, 11 km/sec for Earth re-entry. Now if more energy is required, the entry velocity increases. For the Parabolic transfer the velocity can be larger than 15 km/sec. As the entry velocity increases, the shock and thus the change is thermodynamic properties will change as well. For entry-flights this results in an increase in the heat delivered to the entry vehicle. [Finke (1993)]

To protect the payload from this heat, it is installed with a thermal protection system. There exist two main types of such systems. The first and oldest are ablative thermal protection materials, the second was first used during the Space Shuttle Program and is reusable. These two thermal protection methods are the exact opposite from one another. Reusable thermal protection materials last during their entry flight so that the system can be re-used. While ablators are consumed during flight, this method is older

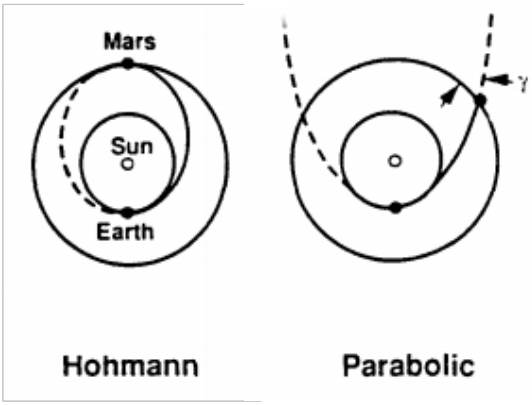

Figure 1.1: Schematic of a Hohmann and Parabolic transfer

than the reusable method. Due to the high velocities of the entry flights of future long distance missions it is predicted that ablative thermal protection materials will be the method of choice. [Laub and Venkatapathy (2003)]

As part of research and development of new ablators this project was set-up. During this project it is aimed to study the gases produced during the consumption of ablating materials. In current ground testing the ablative processes are observed only in the stagnation point, during which it is also assumed that the flow properties are one-dimensional. To improve ground based testing, in this investigation the three dimensional effects of the flow are considered, focusing on the out-gassing phenomena of the pyrolysis process. The question that will be answered in this project is:

Qualitatively characterize off-stagnation out-gassing phenomena.

The project is part of the master program at the Aerospace Engineering faculty at Delft University of Technology and is conducted at the Von Kármán Institute. Chapter 2 gives a short overview of the hypersonic flight regime. The principle of ablative thermal protection materials, a summary of current research and the steps taken in this investigation are discussed in chapter 3. Then the test facility and measurement techniques are discussed in chapter 4, followed by the test and their results in chapters 5, 6 and 7. First the chemical and thermal boundary layer are scanned to identify the main contributors in the flow. Next the presence of CN violet is imaged in specific and finally a seeder technique is discussed to track the internal gas flow in the material. The recommendations and conclusions are given in chapters 8 and 9, respectively.

Chapter 2

Hypersonic Flight

This study is performed in the hypersonic flight regime, when flying in this regime the vehicle is required to protect itself against an extreme outside environment. Anderson (2006) described it as that regime were some from five phenomena become progressively more important, the phenomena are: thin shock layers, entropy layer, viscous interaction, high-temperature flows and low density flows. As the main topic of this study entails the consumption of ablative thermal protection materials, it is the high-temperature flows that are most important. Nevertheless the regime consists of five phenomena, which are therefore discussed below.

As a rule of thumb it is assumed that any flow with a Mach number above 5 is hypersonic, but this is not necessarily true. Unlike when entering the supersonic fight regime where the sound barrier is overcome, there is no distinct phenomenon that clearly dictates the difference between the supersonic and hypersonic flight regime.

2.0.1 Thin Shock Layers

Oblique shock theory says that for any given upstream Mach number (M_1) and surface corner angle (θ), the shock angle (β) and the downstream Mach number (M_2) can always be calculated using equations 2.1 and 2.2 where γ is the heat capacity ratio. A schematic with the above parameters is given in figure 2.1.

$$tan(\theta) = 2cot(\beta)\frac{M_1^2 sin^2(\beta) - 1}{M_1^2(\gamma + cos(2\beta)) + 2} \tag{2.1}$$

$$M_2 = \frac{1}{sin(\beta - \theta)} \sqrt{\frac{1 + \frac{\gamma-1}{2} M_1^2 sin^2(\beta)}{\gamma M_1^2 sin^2(\beta) - \frac{\gamma-1}{2}}} \tag{2.2}$$

From the continuity equation it is known that the density jump across the shock wave increases with increasing Mach number, as shown in equations 2.3, where ρ is the density, M the Mach number, which is equal to the velocity (u) divided by the speed of sound (a). Indices 1 and 2 represent the properties before and behind the shock wave, respectively.

$$\rho_1 u_1 = \rho_2 u_2 \tag{2.3a}$$
$$\rho_1 M_1 a_1 = \rho_2 M_2 a_2 \tag{2.3b}$$
$$\frac{\rho_2}{\rho_1} = \frac{M_1 a_1}{M_2 a_2} \tag{2.3c}$$

As the Mach number before the shock wave increases, so does the density behind the shock wave, which forces the flow to move through a smaller volume. This makes that the shock lies closer to the surface, as indicated in equation 2.4, where $\dot{m}$ is the mass flow, A the cross sectional area, u the velocity and ρ the density. Table 2.1 shows an example of how hypersonic Mach numbers influence the shock angle for a given surface angle, based on equations 2.1 and 2.2. The layer between the shock wave and the surface is called the shock layer, which is thin for hypersonic flight.

$$\dot{m} = constant = \rho(\nearrow) u A(\swarrow) \tag{2.4}$$

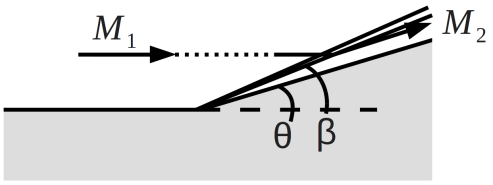

Figure 2.1: Schematic clarifying the parameters

Table 2.1: Hypersonic versus supersonic flight

	Supersonic flight	Hypersonic flight
Upstream Mach number [-]	2	10
Surface angle [degrees]	10	10
Shock wave angle [degrees]	39	15
Downstream Mach number [-]	1.66	6.53

2.0.2 Entropy Layer

Similar to the density, the entropy increases across a shock wave. The magnitude of this jump is dependent on the strength of the shock wave. For hypersonic flight the shock wave is strongest at the vehicle stagnation region. Because the entropy increases according to the strength of the shock, the streamlines passing through the stagnation region have a higher entropy than the other streamlines. This gradient in entropy that exists right after the shock is carried along with the flow generating an entropy layer close to the surface of the body. The layer affects the boundary layer growth and it creates a strong vorticity in this entropy zone.

2.0.3 Viscous Interaction Parameter

Due to the high altitudes at which hypersonic flights take place the free stream density is low and in turn also the Reynolds number (Re) is low, see equation 2.5 with u the velocity, L the characteristic length, ρ the density and μ the viscosity. The low Reynolds number causes the boundary layer to be thick. This forces the the boundary layer and the shock layer to be one and the same thing, causing the entire shock layer to be viscous, which affects the shock wave shape and the surface pressure.

$$Re = \frac{uL\rho}{\mu} \tag{2.5}$$

The high velocity of the flow contains a lot of kinetic energy, which is slowed down in the shock layer due to the viscosity. This loss in kinetic energy is partially transformed into internal energy of the gas, which increases the temperature in the boundary layer and thus also in the shock layer. This affects the viscosity in the flow which in turn affects the boundary layer thickness and the shock wave shape.

2.0.4 High-Temperature Flows

The effect of the viscosity in the boundary layer makes the temperature rise extremely. The temperatures can reach those quantities that force the gas molecules to dissociate, separate into atoms. In some cases, the temperatures can be so high that the flow not only dissociates but also ionizes. But, the viscosity is not the only source of extreme temperatures in the flow. In the nose (stagnation) region of the vehicle, the shock wave is stronger than outside of this region. Here the shock can become a normal shock wave. Due to the strength of the shock wave, the temperature jump is larger than elsewhere around the vehicle.

The high temperature forces the assumptions that were valid during supersonic flight to be revised. For the supersonic regime it was assumed that the capacity ratio (γ) is constant so that the gas can be assumed to be ideal. When the temperature increases as it does in the hypersonic regime, the gas no longer behaves as a ideal gas. First the vibrational energy of the molecules is increased, which causes the heat capacities (c_v and c_p) to become dependent on the temperature of the gas and thus also the heat capacity ratio (γ). For oxygen this occurs at a temperature of about 800K. As the temperature is further increased, chemical reactions start to occur and chemical equilibrium is assumed. This assumption allows the Mach number to be estimated based on the temperature and static pressure in the flow, without investigating the gas composition and state first [Anderson (1964)]. Now the heat capacities and the heat capacity ratio are dependent on the gas temperature and pressure. At this point the molecules dissociate, which happens at about 2500K for oxygen. The higher the temperature gets, the further the heat affects the gas, after the gas was dissociated it ionizes at about 9000K for oxygen. Finally now the oxygen is plasma, the different temperatures and the dissociation zones are indicated in figure 2.7

2.0.5 Low-Density Flow

At sea level the mean free path of the molecules is small so that it is assumed that the gas is a continuum. Now if the altitude increases, the mean free path of the molecules increases to and the continuum assumption becomes questionable. First the no-slip condition at the vehicle surface is no longer valid. At this point, there is a finite velocity at the surface wall, which is called the velocity-slip condition. Now if the altitude increases further, the assumption that the surface temperature and gas temperature at the surface are equal, does not hold up anymore. This is called the temperature-slip condition. At the onset of these conditions the gas is still assumed to be a continuum with corrections for the slip conditions. At even higher altitudes, the continuum is no longer valid. At this altitude the density is so low that only a few molecules impact the surface and the molecules do not impact with each other immediately after impact with

the surface. This is called free molecular flow. The characteristic number that describes weather a flow is rarefied or not is the Knudsen number, which is presented in equation 2.6 with λ the mean free path and L the representative physical length scale.

$$Kn = \frac{\lambda}{L} \tag{2.6}$$

2.0.6 Flight Path

Figure 2.2 shows the main forces that work on an entry vehicle during flight. In the figure, L, D, W, V, θ and r define the main parameters working on the body, these are lift, drag, weight, velocity, flight path angle and radius to the Earth's center, respectively. Equations 2.7 can be derived from the figure, describing the flight path of an entry vehicle, with m the mass of the vehicle and t the unit time. Now assume that for atmospheric entry the flight path angle, θ, is small, so that $sin(\theta) \approx 0$ and $cos(\theta) \approx 1$, see equations 2.8. Also m is replaced by W/g, with g the gravitational acceleration.

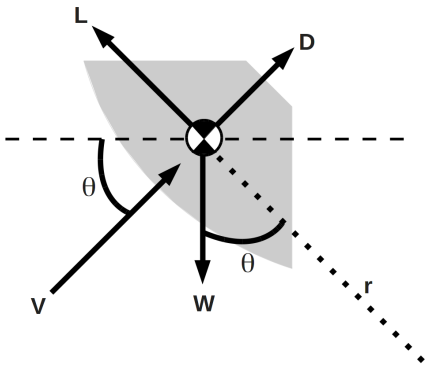

Figure 2.2: Forces working on entry vehicle

$$W sin(\theta) - D = m\frac{dV}{dt} \tag{2.7a}$$

$$L - W cos(\theta) = -m\frac{V^2}{r} \tag{2.7b}$$

$$-D = \frac{W}{g}\frac{dV}{dt} \tag{2.8a}$$

$$L - W = -\frac{W}{g}\frac{V^2}{r} \tag{2.8b}$$

Finally the drag (D) and the lift (L) are replaced by their respective definition so that the equations are a function of the drag and lift coefficient, D = $1/2\rho$ S V^2 C_D and L = $1/2\rho$ S V^2 C_L. For the drag the result is given in equations 2.9 and for the lift in equations 2.10. Equation 2.9b describes the no-lift fight path. The parameter, $\frac{W}{C_D S}$ is called the 'ballistic parameter' since it is the only parameter that describes the flight path in case of a ballistic entry. Similarly equation 2.10b describes the flight path, but

only if the vehicle is a lifting body, with $\frac{W}{C_L S}$, the 'lift parameter'.

$$-\frac{1}{2}\rho S V^2 C_D = \frac{W}{g}\frac{dV}{dt} \tag{2.9a}$$

$$-\frac{1}{g}\frac{dV}{dt} = \left(\frac{W}{C_D S}\right)^{-1}\frac{\rho V^2}{2} \tag{2.9b}$$

$$\frac{1}{2}\rho S V^2 C_L - W = \frac{-W}{g}\frac{V^2}{r} \tag{2.10a}$$

$$1 - \frac{1}{g}\frac{V^2}{r} = \left(\frac{W}{C_L S}\right)^{-1}\frac{\rho V^2}{2} \tag{2.10b}$$

Ballistic (Re-)Entry Flight

The ballistic parameter describes the flight path for a ballistic entry flight as mentioned before. This parameter also indicates the magnitude of the deceleration and heating of the vehicle as the flight progresses. A low weight and/or low drag and a large frontal area result in a low ballistic parameter and less intense heating and deceleration since the air is thin at high altitudes. The opposite applies to a high ballistic parameter.

The earliest hypersonic vehicles, ballistic missiles, used this flight method. To protect the missile from the heat created during flight, they were installed with thick heavy metallic heat shield that functioned as a heat sink for the short heating pulse at high altitudes. To increase the accuracy of the missiles, the ballistic parameter was increased and the missile shape a blunted sphere-cone. This increased the impact velocity allowing the descending phase to be less dependent on winds. Now the heating was higher, so that a new method needed to be employed for the thermal insulation of the missile. For this material at the surface of the heat shield was allowed to melt or vaporise, which transfered the heat back into the atmosphere. This method of thermal protection is also known as ablation.

An example of the flight trajectories using a ballistic entry are given in figure 2.3. In the figure the altitude, in kilo-feet, is plotted against the flight velocity in feet per second. The different lines in the plot represent different ballistic parameters ranging from 100 to 5000 pound force per feet squared. The lower values (100 and 500) represent the early missile shaped using a heat sink as thermal protection system. While the higher values represent the missiles using ablative thermal protection systems. Notice how the arrival velocity at sea level increases with increasing ballistic parameter, which is consistent with

the above. Figure 2.4 presents the stagnation point enthalpy for the different ballistic parameters, which shows that the higher the ballistic parameter, the higher the stagnation point enthalpy and thus also heating. This is also consistent with the above statements.

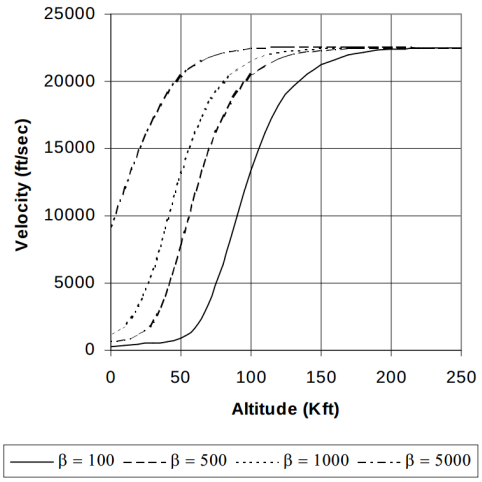

Figure 2.3: Altitude versus Velocity plot for ballistic entry flights [Adams]

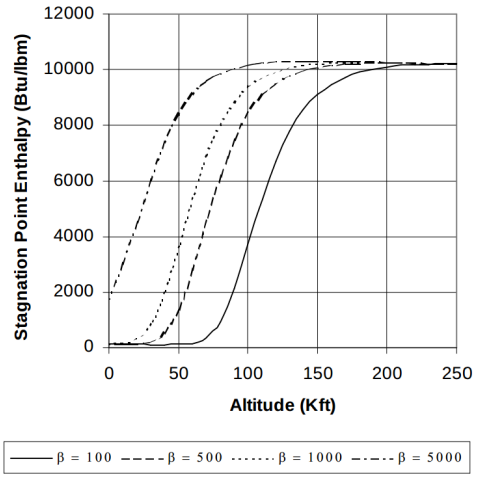

Figure 2.4: Altitude versus Stagnation point enthalpy plot for ballistic entry flights [Adams]

In 1962, the first manned ballistic re-entry flight of the "Friendship 7" Mercury capsule brought Colonel John Glenn back from space. The flight had a ballistic parameter of 54.98 [lbf / ft^2] and entered the atmosphere at an altitude of 250 000 ft with a velocity of 23 000 ft/sec. During his flight Colonel Glenn experienced a deceleration of 8 g's over a 30 second period. The incentive to decrease the experienced g loads by the passengers lead to the development of a lifting entry for manned flights. [Adams]

Lifting (Re-)Entry Flight

Different from a ballistic entry, during a lifting entry the flight path can be adjusted at all times so that there is more control on the vertical motion and the flight direction of the vehicle during its descend. This is similar to a gliding flight without the heating and high velocities. As mentioned above, the reduction of the g loads during flight was the incentive in the development of this entry method. It is therefore that the lift to drag ratio is the primary design parameter. Lower values of this value give moderate g's, moderate heating and low maneuverability. High values result in low g's but very low flight duration and continuous heating.

Although the peak heating of the lifting re-entry is lower than that of the ballistic re-entry, the total heat the needs to be absorbed over time is higher, this is due to the elongated flight duration of the lifting flight. Figure 2.6 presents the stagnation point

enthalpy for a lifting re-entry at different flight path angles, from the gradient in the image it can be seen that the heating of the vehicle is extended over a longer period of time compared to the ballistic flights. Secondly in this figure it can be seen that the heating now occurs at an altitude of 200 000 ft, while this was 100 000 to 150 000 ft for a ballistic re-entry. Different from the ballistic flight of Colonel Glenn, the lifting entry of the Space Shuttle orbiter experienced g loads ranging between 0.5 and 1. The flight velocity of lifting re-entry flights is given in figure 2.5, comparing this figure to the one representing a ballistic flight a difference in slope can be seen in the curves. This change in slope implies that the deceleration is less intense for the lifting flight.

Finally in the figures it should also be noticed that for the largest flight path angles the vehicles trajectory starts oscillating. Entering the atmosphere at a too high flight path angle can even lead to skipping out of the atmosphere back into space. This shows the sensitivity of the lifting flight to the flight path angle.[Adams]

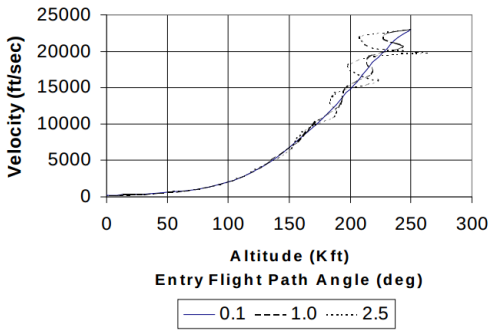

Figure 2.5: Altitude versus Velocity plot for lifting entry flights of the NASA Space Shuttle [Adams]

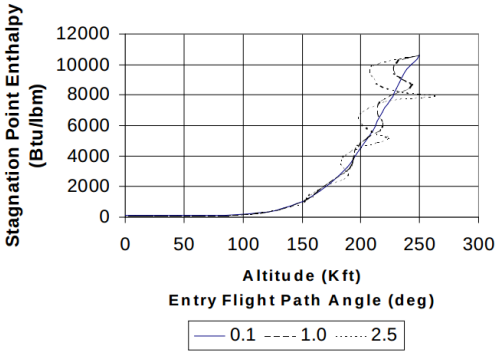

Figure 2.6: Altitude versus Stagnation point enthalpy plot for lifting entry flights of the NASA Space Shuttle [Adams]

Velocity - Altitude Maps

Altitude-velocity maps are used to present the flight path of an atmospheric entry flight. Figure 2.7 shows such a map for the lifting entry flight of the Space Shuttle; which enters the atmosphere from orbit. As the shuttle travels deeper into the atmosphere it is slowed down due to aerodynamic drag. The larger the characteristic parameters, ballistic and/or lifting parameter, the deeper the vehicle will penetrate the atmosphere before being slowed down. Superimposed on figure 2.7 are the regions associated with chemical reactions during flight. On the top of the figure there are two percentages, 10 and 90, these indicate the beginning of the reaction, when 10% of the gas has experienced the reaction and the end of the reaction, when 90% of the gas has changed. The entry path of the space shuttle (indicated in the figure) crosses a large amount of these regions.

The shuttle will encounter, dissociated oxygen and nitrogen and increased vibrational excitation of the molecules in the flow. Due to the large interaction of the flow with these chemical zones, the importance of the high temperature effects becomes clear.

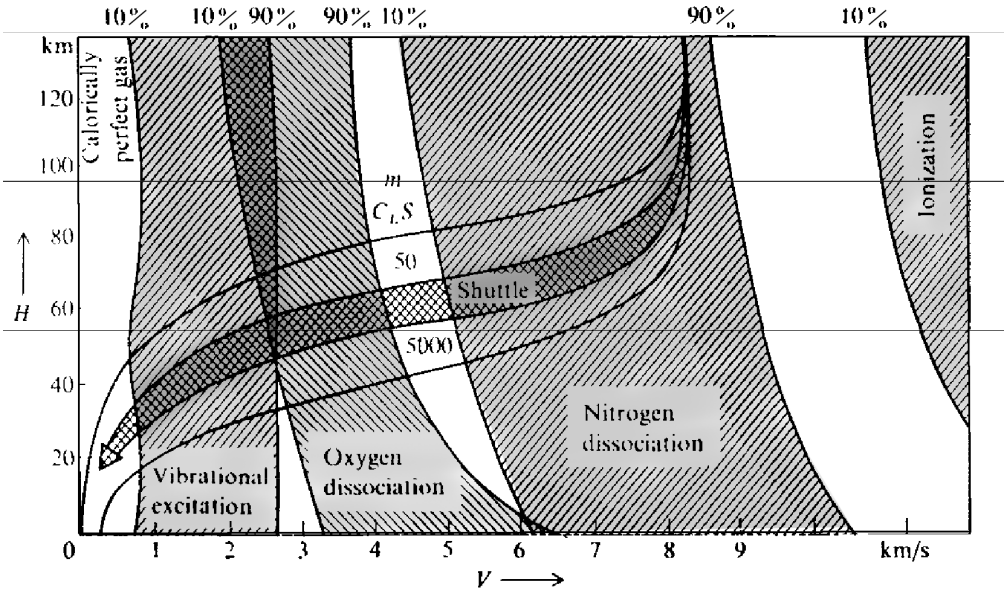

Figure 2.7: Velocity-Amplitude map [Anderson (2006)]

Chapter 3

Ablative Thermal Protection Materials

This chapter gives a detailed description of the working principle of ablative thermal protection materials. Also a numerical investigation on the transport phenomena in the material and the common experimental measurements are presented.

3.1 Working Principle of Ablative Materials

Ablative thermal protection materials are the oldest of thermal protection materials. As they come into contact with the high temperatures of hypersonic flight the material allows itself to experience physical and chemical changes leading to the consumption of the material and the insulation of the vehicle payload. The idea of ablators was first described by R. Goddard in his 'Report Concerning Future Developments', here he explains how meteors are affected by the atmosphere upon entry. [Goddard (1920)]

In its most basic form the material has two components, a carbon fiber structure and an organic filler, such as certain types of wood, such as chinese oak or cork. The structure is brittle, lightweight and porous so that it can hold the filler. Figure 3.1(a) shows the top view of a preform test sample which is made only out of carbon fibers and thus it is only the structure and figure 3.1(b) on the other hand shows a virgin cork ablator. Cork is a natural ablator and contains a lot of organic resin. With this image it is aimed to show the difference between just the carbon structure of ablative thermal protection materials and the complete material impregnated with an organic filler such as phenolic.

As the material comes into contact with heat the organic filler will react to the increase in temperature first, this is called pyrolysis and is elaborated in section 3.1.1. After this

(a) Top view of preform test sample

(b) Front view virgin Monolithic ablator

Figure 3.1: Example of two material components

only the carbon structure remains with a carbon char layer that was deposited during pyrolysis. This carbon layer is now in direct contact with the high temperature flow and also reacts with it so that the surface recedes. This is called ablation and is explained in section 3.1.2. Figure 3.2 shows the different steps in the pyrolysis and ablation processes. A third process that might occur is catalycity, which is also the only process that can occur with reusable materials, for which the process can lead to increased heat, see section 3.1.3. [Laub and Venkatapathy (2003); Panerai (2012)]

3.1.1 Pyrolysis

Pyrolysis is a process that only occurs in ablative materials, as is written before these materials protect the payload by allowing themselves to be consumed. For the material to work optimally, the reactions experienced by the materials should be endothermic. This means that the heat from the surrounding is used to force the material to chemically change. Below, the pyrolysis reactions are listed. [Helber et al.; Uhl and Fletcher (2010)]

1. As the material is exposed to the high enthalpy environment the organic resin will sublimate or evaporate. This creates gas inside the sample, which is pushed outwards due to the increase in pressure.
2. As the organic resin becomes a gas, some char is left behind in the material and on top of the surface. During these first two steps the material can loose up to 50% of its original mass.
3. When the released gases come into contact with the free stream flow, it can occur that the atoms chemically start to react to each other. This is not necessarily a

positive effect on the consumption of the material. Often the energy that was required to dissociate an atom is released again as the atoms combine into molecules.

4. The gases leaving the material flow against the free stream flow direction and because the pyrolysis gases are considerably colder than the free stream, a cold gas layer is created around the sample. Generally this layer acts as an insulator and protects the material from the environment and thus ensures a reduction of convective heat to the surface.

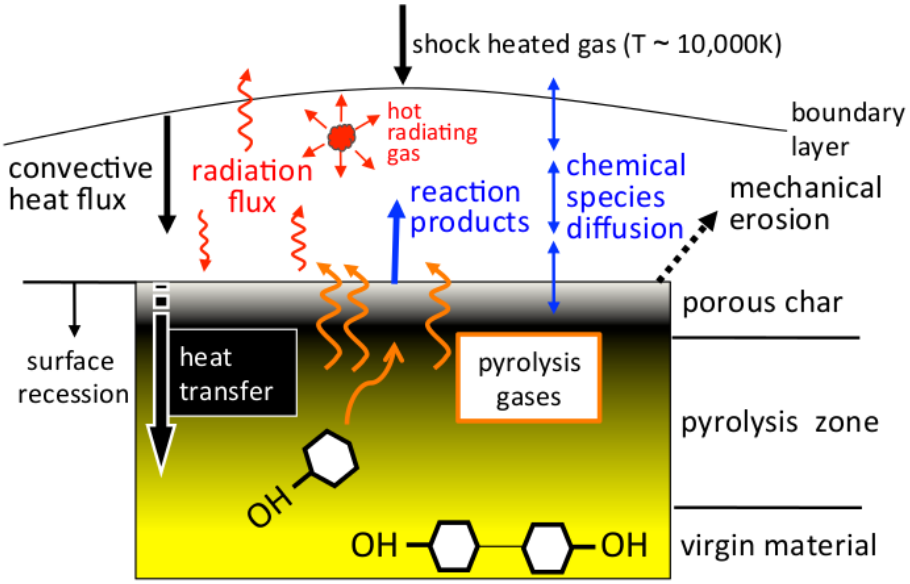

Figure 3.2: Pyrolysis and ablation processes of an ablative thermal protection material [Helber et al.]

3.1.2 Ablation

The ablation process also only applies to ablative materials, as the names suggest. As the pyrolysis process continues, it decreases in strength. The more organic resin is removed from the material, the less left over virgin resin there is, see figure 3.2. The left-over char layer is now in direct contact with the high temperature gas because the pyrolysis gases no longer offer a cold insulation. At this final step, the material can experience three things, heterogeneous chemical reactions with the free stream plasma flow (oxidation or nitridation), a phase change (sublimation) or mechanical failure (erosion). One of the possible chemical reactions is an oxidation of the carbon surface. In general the

oxidation reaction is exothermic and thus increases the convective heat at the surface. The preferred reactions are phases changes, even though they lead to a consumption of the material, they are endothermic and thus absorb heat in order to occur. At this point catalycity also plays a major role in the amount of convective heat delivered to the surface. [Uhl and Fletcher (2010)]

3.1.3 Catalycity

As already previously stated, during (re-)entry a significant number of molecules are dissociated into atoms. This is an endothermic process and thus, heat energy is consumed. When these atoms hit the material surface, recombination into molecules is promoted, this is heterogeneous catalysis. As the atoms recombine on the surface, they emit the heat energy that was previously absorbed to dissociate the molecules (exothermic).

Since the first use of heat shields, this has played an important part in the design and sizing of thermal protection systems. The amount of recontaminating atoms is dependent on the surface temperature, the surface roughness and the accommodation of chemical reactions amongst other. Because this process is still not well understood since its first discovery, the assumption that all thermal protection materials are highly- or super-accommodating is still in practice. Catalycity (γ) is defined as the ratio between the flux of recombining atoms of species i ($\mu_{i,rec}$) and the flux of impinging atoms on the surface (μ_i), equation 3.1. So that $\gamma = 1$ represents a fully-catalytic surface and $\gamma = 0$ a non-catalytic surface. [W. G. Vincenti and C. H. Kruger, Jr. (1917)]

$$\gamma = \frac{\mu_{i,rec}}{\mu_i} \tag{3.1}$$

3.2 State of the Art: Numerical Modeling

The purpose of a numerical model is to describe the flow and material and their interactions as they would be in real flight conditions or experimental testing. The governing equations consist of mass conservation, momentum conservation in porous media and energy conservation. The momentum conservation is specified to porous media since the ablators become porous as pyrolysis progresses through the material. The boundary conditions that complete the numerical model include a surface energy balance which describes the interaction between the flow and the material at the wall and a surface mass balance and recession rate which describes the ablation rate of the material. The result of the numeric simulation is dependent on the accuracy of the physics describing the ablation processes. Due to limitations in the computational power, the models are simplified. When the accuracy and time cost are traded off against each other the model can be validated based on experimental test results. Finally after the validation, the model can be used to simulate new test conditions that otherwise would result in expensive experimental tests. The most difficult part of modeling ablation is the coupling between the material field and the flow field. [J. Lachaud (2011)]

In this section a numerical modeling study is discussed. According to the results of this investigation, the transport phenomena in the test sample should be modeled using a multi-dimensional model instead of the commonly used one-dimensional model. The investigation raises questions on the side-wall and inflow effects in the ablator due to the pressure decay in the material as pyrolysis progresses.

According to Weng et al. the modeling of the material flied should be according to a three-dimensional model instead of a one-dimensional. As stated above compromises need to be made in the modeling due to time costs. One of these simplifications can be the reduction of a multi-dimensional problem to a one-dimensional problem. To asses the effect of this simplification of the results of the simulation, Weng et al. made a comparative study. According to this study the one-dimensional model indicates that the pyrolysis gases flow out through the front surface, while the three-dimensional model results indicate something completely different. For the one-dimensional model the side walls were assumed to be impermeable forcing the gases to flow out the only left permeable wall, the front wall. For the three-dimensional models all walls were allowed to be permeable. This change also changed the results drastically, initially the gases do indeed flow out through the front wall, but as the simulation progressed and the material became porous the gases used an alternate route. Now the free stream enters the porous part of the material and the pyrolysis gases blow out through the side walls.

Weng et al. created plots presenting the comparison of the one-dimensional or impermeable test cases (case one) and the three-dimensional of permeable test case (case two), these are presented in figure 3.3. The figure shows the flow inside the material and

is composed of streamline plots at 20, 40 and 60 seconds in the the simulation. The left column presents the one-dimensional case and the right the three-dimensional cases. Looking at the plots it is immediately clear that the effect of the dimension is enormous. The streamlines of the one-dimensional case do not show anything unexpected, the streamlines are vertical and point towards the front wall where all the gases leave the material. For the three-dimensional case, at the top of the material the streamlines point from a horizontal line in the material. Deeper in the material it is indicated that the flow originates from this line and flows further through the material and out through the side walls. The second figure, figure 3.4 shows the mass flux for both test cases at the front (left) and side (right) wall of the sample at different time instances. The left plot in this figure shows the result for the one-dimensional flow, where there is only flow at the front surface which decreases over time. This is expected as the side walls are defined as impermeable. For the three-dimensional case with permeable side walls (right) the flow through the side walls is larger than the flow through the front wall indicating that the side wall effects are significant. As the pressure in the material decreases further there can even be inflow through the front wall which is also not indicated by the one-dimensional model. [Weng and Martin (2013)]

This investigation shows that three-dimensional effect play a vital role in the performance of thermal protection materials. In this study it is aimed at characterizing the side wall flow experimentally and develop a side wall testing method, so that the effect can be fully understood and help validate new numerical models.

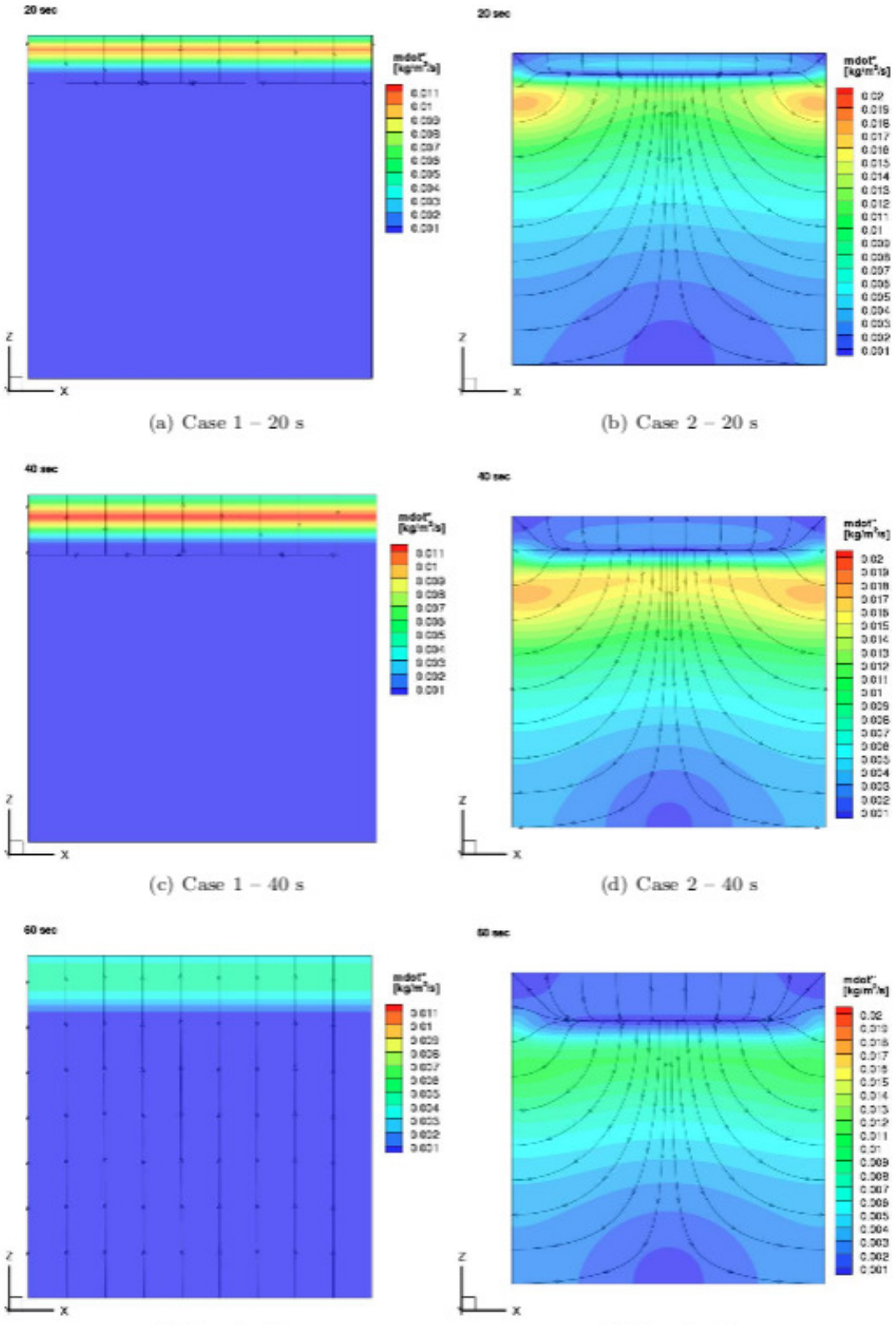

(a) Case 1 – 20 s (b) Case 2 – 20 s

(c) Case 1 – 40 s (d) Case 2 – 40 s

(e) Case 1 – 60 s (f) Case 2 – 60 s

Figure 3.3: Streamline plots of test case one (left column) and case two (right column) after 20, 40 and 0 seconds

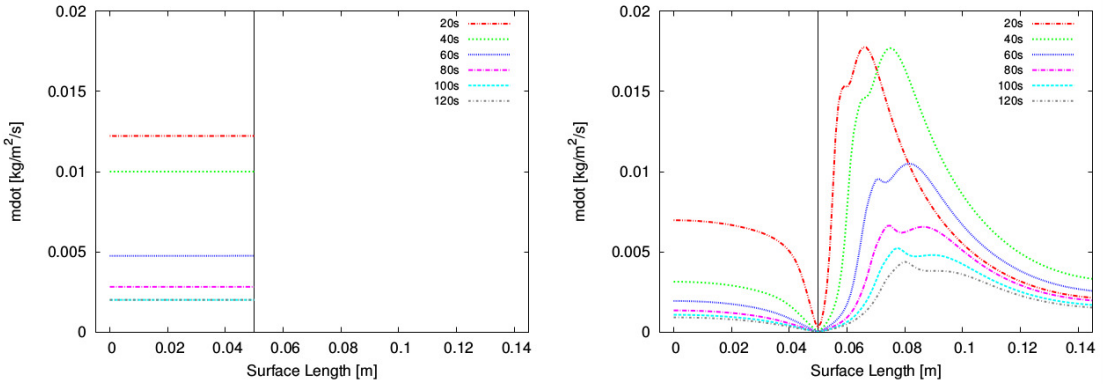

(a) Case 1 – Cylinder, impermeable side

(b) Case 2 – Cylinder, permeable side

Figure 3.4: Surface normal blowing mass flux for case one and case two; the black line indicates the separation between the front surface, to the left, and the side surface, to the right

3.3 State of the Art: Experiments

During the design and development of thermal protection materials and systems, many different aspects have been investigated to give a better understanding of the materials and what happens to them in flight. The information is split up into their region of interest.

Experimental testing results are often used together with numerical simulations. To allow an easy transfer between these two fields it is aimed to use test samples with a geometry that will remain the same durng testing. To acchieve this the shape should be such that the heat flux is the same for the entire frontal surface. Often this is acchieved by using an iso-q shaped test sample. An example of an iso-q shape is given in figure 3.5, the shape is build up from a ellipsoid and a cylinder.Another common test sample shape is compused of a hemi-sphere and cylinder, but this shape knows a higher heat flux augmentation at the shoulder of the sample than the iso-q shape, and is therefore less favorable. [Milos and Chen (2009); T. van Eekelen (2004)]

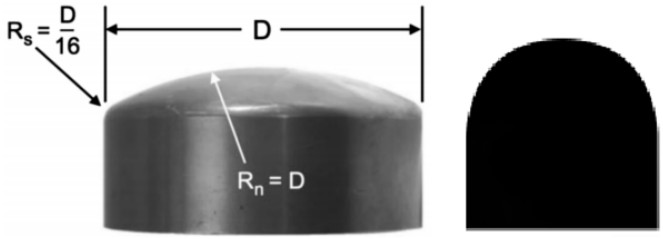

Figure 3.5: Example of an iso-q (left) and sphere-cyliner (right) shape

3.3.1 Stagnation Point Testing

In various literature it is said that the stagnation region is of most interest since usually this is the area that receives the highest heat flux in real flight. Due to this high heat flux, this is also the region where the surface will recede the most, which is a critical design requirement of the thermal protection system. [F. S. Milos (1999)]

Surface Recession Determination

The recession of the surface is a direct consequence of the ablation process. As the material is consumed by pyrolysis and ablation, see sections 3.1.1 and 3.1.2, first mainly mass is lost. When ablation becomes the dominant process both volume and mass are lost. The volume is lost at the surface, making the surface recede. The rate at which

this occurs is called the surface recession rate and this is a major design parameter for thermal protection materials. Depending on the flight conditions a certain heat flux is delivered to the material, considering the known recession rate the minimum amount of thermal protection material that is needed.

Absolute Measurement A first and simple way to measure the recession of the material, is by measuring the size before and after testing using a caliper. This method is very easy and fast, but care must be taken when handling the sample. After testing the remaining material is very brittle, if too much pressure is applied to the material the char layer will simply be crushed. Also this method only offers an absolute amount of surface recession, while the interesting part is to see at which point in time most of the surface is lost. Also, due to the shape of the test sample it is difficult to measure the surface recession in other locations than the stagnation point. While it is expected that this region will loose the most surface, it is not necessarily true. [Helber et al. (2014)]

Time Resolved Measurement A time resolved measurement gives the recession over time, which offers the user to obtain more information on the recession of the material surface. Using such a technique, the moment at which the surface recedes the fastest can be identified.

Winter et al. described a newly developed remote recession sensing technique, where a tracer material is inserted in the test sample at a chosen depth. As a base material it was chosen to work with PICA (Phenolic Impregnated Carbon Ablator) because of its easy handling characteristics and limited amount of constituents, which minnimized the amount of added emissions to the spectra. The tracer material were worked into a rod which could then be easily inserted in holes drilled in the PICA sample. To seal off the seeder from the surface, the holes were filled up with a PICA like paste. An example of the placement of the seeder rods into the PICa before sealment is given in figure 3.6. The materials used for the seeder were NaCl (sodium-chloride) and MgCl (magnesium-chloride). For the measurment technique to work the seeder materials should have similar thermal properties, evaporation and sublimation temperatures, as the base material.

The measurement was perfomed using emission spectroscopy since this method can measure emission wavelengths over a wide range (200 - 900 nm). This makes it easy to identify the different species in the flow at a time instance. The tracer elements were required to have a strong and characteristic emission lines when measured so that there presence could be recognised beyond doubt. Figure 3.7 shows an example of the measured spectrum with the theorectical emisson lines of sodium and magnesium superimposed on the plot. From this figure it can be seen that the strong emission lines correspond with some of the peaks in the measured spectrum, but the weaker lines to not show up. As the test sample with the hidden tracer materials is inserted into the plasma flow the

surface will recede and after some time the seeder material will become the surface of the test sample. This is measurement one. As the recession continues the material will disappear again after some time, measurment two. combining these measurment point a recession rate can be deduced. Figure 3.8 presents the intensity of the main magnesium and sodium peaks over time. From these lines it can be seen that indeed after some time both species enter (after about 1 second) the flow and then disappear again as the seeder is completely consumed by the heat (after about 4 seconds).

This remote recession sensing offers a greater accuracy compared to the above described absolute measurement, as it is not required for the user to handle the test sample. This does not mean that the test sample is not compromised, for the implementation technique described by Winter a hole is drilled in the test sample to insert the tracer material and it is filled up again with a paste similar to the original test sample material, but not identical. It is unsure how the change to the surface integrity affects the thermal performance of the test sample. In the conclusion of the paper Winter also indicated that the technique could be tailored to focus on the pyrolysis gases. For this alteration the seeder materials should have low pyrolysis temperatures, similar to the temperature at which pyrolysis occurs. [Winter et al. (2014)] As the objective of this project is to explore the side wall blowing, it is aimed to indeed make this alteration to the measurement technique developed by Winter et al.

A more common set-up is to image the test with a high speed camera over the entire duration of the test. Depending on the required level of accuracy and the ablation velocity of the test sample, the camera settings, such as exposure time and frame rate, can be selected. Here it is assumed that the flow and recession is axis-symmetric. By post-processing the images the recession can be followed over time. The advantage of this method is that it is very accurately time resolved and the material integrity is not compromised. It does require a lot of time to set-up, calibrate and post-process though. [Helber et al. (2014)]

Figure 3.6: PICA cylinder with seeded material before sealing

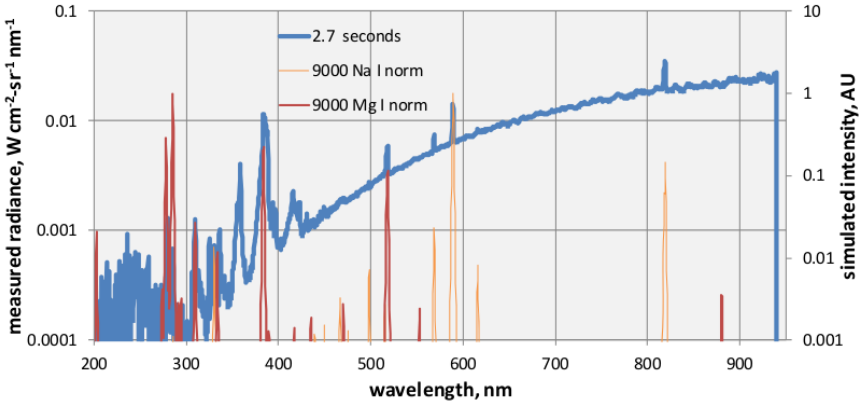

Figure 3.7: Measured spectrum 2.3 seconds after insertion compared to the theoretical spectra of sodium and magnesium

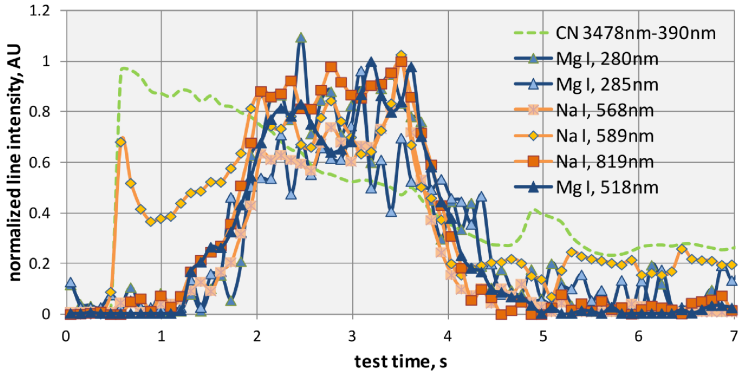

Figure 3.8: Time trace of spectrally integrated line emission of sodium and magnesium

Thermal performance

By placing thermocouples in the test sample, at specific locations, a temperature profile with respect to time is acquired. Placing multiple thermocouples at different depths in the test sample, information can be obtained on the spreading of the heat through the sample. When the test sample is injected the temperature increases faster close to the surface. After some time an equilibrium is reached and all the thermocouples measure the same temperature.

Before the test sample is injected in the plasma jet, often the heat flux is measured first using a calorimeter. Depending on the test conditions the surroundings in the test chamber will heat up, which might cause the test sample to pyrolyze prematurely, this is called preheating. The premature pyrolysis makes the test sample to lose mass before the test has begun, corrupting measurements such as boundary layer characterizations using spectroscopy or surface recession measurements. Due to the premature pyrolysis, the spectroscopy will measure the species as if the test was already further along than it actually is. The surface recession rate could result in a higher or slower rate than normal. A solution is to store the test sample in a water-cooled box in the test chamber until injection. The cooling will prevent the material from premature pyrolysis. [Helber et al. (2014); Covington et al. (2008)]

Test Medium Influence

For air and nitrogen plasma jets resulting in the same surface temperature ($T_{S,max} = 2800K$), the recession rate in air is many times higher than in nitrogen. At these temperatures, the oxygen in the air is almost fully dissociated which allows for a rapid consumption of the char layer by the oxygen atoms. Secondly, the mass loss for both cases remains similar. Mass loss in carbon phenolic ablators is generally caused by internal evaporation of the filler (pyrolysis), which is independent of the test medium and dependent on the testing temperature. While mass loss associated with recession of the char layer is dependent on chemical reactions and shear stresses in the boundary layer. [A. Martin (2010); E. W. Lemmon (2000)]

Boundary layer Species

The species in the boundary layer are observed. This is done using spectroscopy, which observes the wavelength at which each species emit light. From the wavelength the species can then be identified, as was already explained in section 4.2. From these measurements, not only the different dominating species can be determined, but they can also be measured over time across the scope of the test. This can tell the user if the species are formed because of the pyrolysis or if they are part of the ablation process. According to Helber, the main species identified with gas-phase radiation are molecular carbon, C_2 Swan, and CN violet. C_2 Swan in named after physicist W. Swan who studied

the spectral response of diatomic carbon. Both these species are strong radiators, even when a small amount can easily be detected. The amount of these species present in the boundary layer is dependent on the test gas. This is mainly the case for CN, as there simply are less nitrogen atoms in an air plasma. CN violet is identified during pyrolysis and ablation, while C_2 Swan is assumed to be a pyrolysis product.

In a test performed by Helber et al, the test sample was subjected to a 3MWm^{-2} heat flux. During this test the initial internal temperatures registered by thermocouples exceeded 500 K due to the heat radiating from the hot plasma jet, see figure 3.9. At the time when the species were first observed, the surface temperature (measured with a pyrometer) was still too low for the carbon in the sample to sublimate ($T > 3000\text{K}$ [S. M. Scala (1965)]). Therefore it was concluded that they must be pyrolysis species. The phenolic resin ($C_6H_5 - OH$) in the test sample decomposes into multiple hydrocarbon molecules, especially the contribution of acetylene, C_2H_2, is important. The two carbon atoms in the acetylene are bonded with a strong triple bond. At higher temperatures the molecule will decompose into C_2 and $2H$. So, when $2H$ is measured by the spectrometers it always is a pyrolysis product. For oxygen plasma the hydrogen atom can also combine with an oxygen atom from the plasma flow. This creates a third pyrolysis species, OH. As a direct result of the decomposition of the phenolic resin CH is formed. [Panerai and Chazot (2012); Sakraker and Asma (2013); Helber et al. (2014)]

3.3.2 Parallel Flow Testing

Outside of the stagnation point the thermal protection system will also have to endure aerodynamic heating. This heating is less severe compared to the heating in the stagnation point region, but this goes together with increased shear stresses due to the tangential flow velocities at the surface. Thermal protection systems are build out of smaller pieces that are then jointed together. With parallel flow tests the joints between these pieces are subjected to the high enthalpy and shear stress environment that they would encounter during flight as well. These tests mostly serve to check the quality of the system manufacturing. The test samples used for these type of tests have a rectangular shape and can also be installed with thermocouples. [Bouilly et al. (2006)]

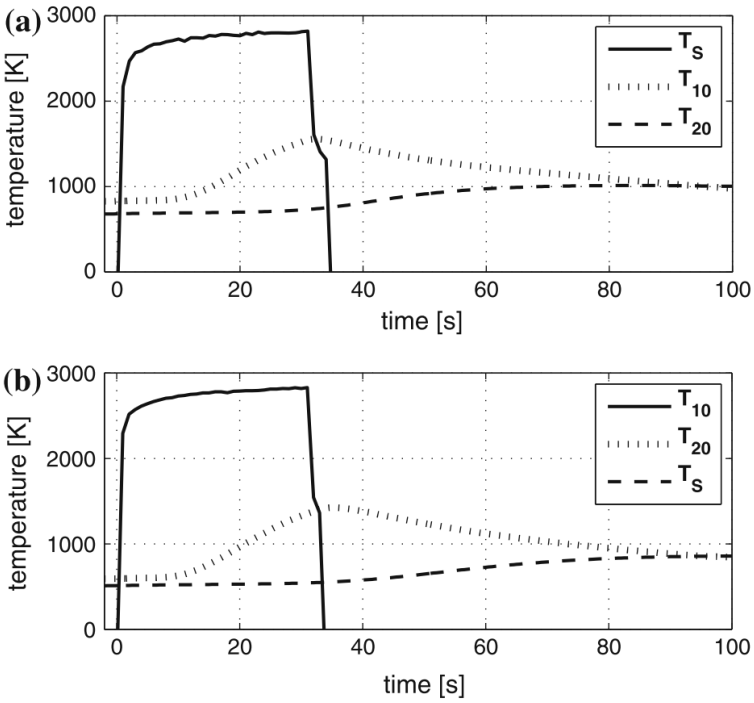

Figure 3.9: Surface (T_s) and internal temperature responses (T_{10}: 10 mm, T_{20}: 20 mm from the initial stagnation point) of ablator in air (a) and nitrogen (b) plasmas [Helber et al. (2014)]

3.4 Plan of Approach

In section 3.2 the paper from Weng describes how the dimension of the modeling of ablative thermal protection materials influences their response to the flow significantly. For a one-dimensional model, the pyrolysis gases blow out only through the front wall. This is however misleading. A three-dimensional simulation also performed by Weng showed that the gases produced during pyrolysis flow out through all walls of the test sample. It is even so that the largest amount of the gases flow out through the side walls of the test sample. As the pyrolysis progresses through the material the flow through the front wall becomes weak and there will be inflow through this wall. From this investigation the importance of the side wall flow has been stressed, while in most of the literature the focus is placed on the stagnation point region. The stagnation point receives the highest heat flux and thus also knows the highest amount of surface temperature, which will lead to a higher recession rate compared to the other side walls. Due to the vast amount of research performed in this region it is well understood and can be used to perform simulations and experiments representative to real flight.

During this project if is aimed to step outside of this region and investigate the outgassing phenomena at the side walls of test samples, so that the ground testing of ablators can be improved. By understanding all the processes in all regions of the thermal protection materials it is hoped that ground testing methods can be improved and models can be adjusted so that they describe the reality more closely.

This will be executed in three steps, first a general impression is obtained from the flow outside of the stagnation point, by observing the flow in the thermal and chemical boundary layer using emission spectroscopy. It is chosen to use emission spectroscopy since this technique offers a wide range of visible wavelengths. During this part of the project both spatial and temporal measurements are made. A more elaborate explanation and test results are given in chapter 5.

The second part of the project focuses on one species but observes it over the entire boundary layer. The contribution of CN violet in all regions of the test sample is investigated. It is chosen to perform this second test campaign to compare the processes at the stagnation point and the side walls at the same time and to compare the difference between pyrolyzing and non-pyrolyzing materials. Because of the amount of information obtained when observing the flow around the entire test sample it is chosen to focus the attention on one species that is known the be a product of both pyrolysis and ablation, see section 3.3.1. The measurement technique used at this stage is a filtered high speed camera. The filter allows the camera only to observe the light emitted by CN violet. The complete explanation and results are given in chapter 6.

Finally, the last step in of this project aims at tailoring the measurement method devel-

oped by Winter so that it allows the tracking of pyrolysis gases, as explained in section 3.3. First an assessment is made to find materials with similar thermal properties as the pyrolysis gases and a clear characteristic emission signature. Once suitable materials are found they are inserted in a test sample and tested. This final test is performed as proof of concept. Because the presence of the seeder materials needs to be identified out of the other species in the boundary layer, it is chosen to work again with emission spectroscopy. The test results are given in chapter 7.

Before the tests and the test results are discussed, the test facility and measurement techniques are presented in the following chapter.

Chapter 4

Test Facility and Measurement Techniques

The facility and measurement techniques used during this project are presented here. The plasmatron is a high enthalpy wind tunnel that allows thermal protection materials to be partially subjected to (re)-entry test conditions. Its main advatage over other high ethalpy facilities is the high purity of the plasma flow. The measurement techniques used are emission spectroscopy, high speed camera imaging and water cooled calorimeter measuring. The first two are used to observe the flow, while the calorimeter is used to ensure the sample is subjected to the correct heat flux.

4.1 Von Kármán Institute Plasmatron

Real hypersonic flight knows high velocities and temperatures due to these velocities. When recreating these conditions in ground based test facilities compromises need to be made, often these two characteristics are split up and tested separately. As already mentioned before, during hypersonic flight a shock wave is present in front of the vehicle. The region before the shock wave is considered the high velocity region. Here the Mach number is considerably higher than behind the shock wave, as shown in table 2.1. Due to the shock wave the flow properties undergo a sudden change, one of the direct effects is that the temperature behind the shock is many times higher than in front of the shock, as explained in section 2.0.4. It is therefore that the region behind the shock wave is considered as the high temperature region. In this project the effect of the flow around the body on the material is investigated and thus only the high temperature region is of interest.

The Plasmatron generates a plasma torch that is projected into the test chamber, gen-

erated by inductive heating, this is represented in figure 4.1. A coil (inductor) is placed around a quartz tube through which the cold gas flows. By allowing high-frequency and high-voltage currents to run through the coil (High Frequency generator, HF) an induced electric and magnetic field is generated in the center of the quartz tube. The time dependency of the induction allows for a periodic variation to occur, this then causes free electrons to move in the gas creating current loops. Finally these loops heat the gas by means of Joule heating, $Q = RI^2t$, with Q the added heat, R the resistance of the system, I the current running through the system and t the operation time. As the gas heats up, it goes through a chemical change. The molecules dissociate into there respective atoms and these ionize creating plasma.

From the above description it is clear that the gas and the inductor are not in direct contact. This is one of the main advantages of the Plasmatron as it ensures a high gas purity. The wind tunnel at the VKI was designed and build to meet the need of development tools for future European space missions. It offers a test environment that allows the user to simulate thermal entry conditions for the design, testing and verification of thermal protection materials (TPM) used in real flight applications. The Plasmatron allows plasma based on argon, nitrogen, carbon dioxide, air or a mixture of gases up to temperatures of $1000K$. The test chamber is kept at pressures below the atmospheric pressure, ranging from 5 and $200mbar$. [Bottin et al. (1999)]

Figure 4.2 presents the schematic of the entire test facility, while figure 4.1 only shows the plasma generation. From figure 4.2 it can be seen that the operator can use the facility through the control, which operates the transformer. This controls the valves for the vacuum pump and the cooling system, the spectrometer and the direct current current generator (DC) and high frequency generator (HF). The gas (center-left in the image) flows from three tanks, representing the three possible test gases, through the plasma generator into the test chamber. The exit nozzle of the test chamber leads to a cooling tank (H/X) and finally the left over heat is removed through the roof (stack). Also, the image shows that the cooling circuit is closed. The facility offers optical access to the test chamber through quartz windows. Quartz is a very reliable material that can cope with the difference in the surroundings inside and outside of the facility without cracking and if offers a wide range of wavelength transmittance, figure 4.3. The Plasmatron operating envelope compared to Earth (re)-entry flight trajectories is presented in figure 4.4. [von Kármán Institute for Fluid Dynamics]

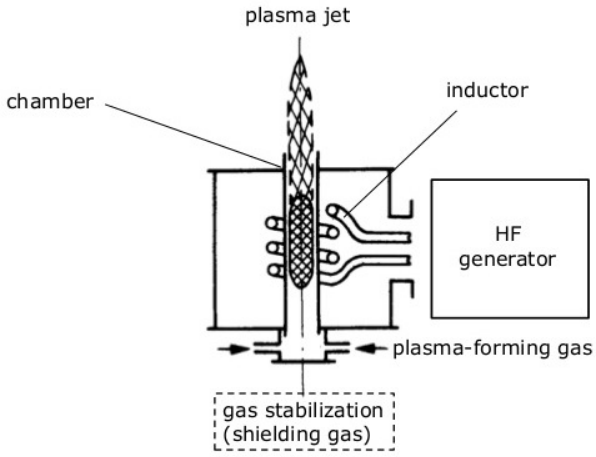

Figure 4.1: Schematic of Plasmatron heating mechanism [Rydkin (2012)]

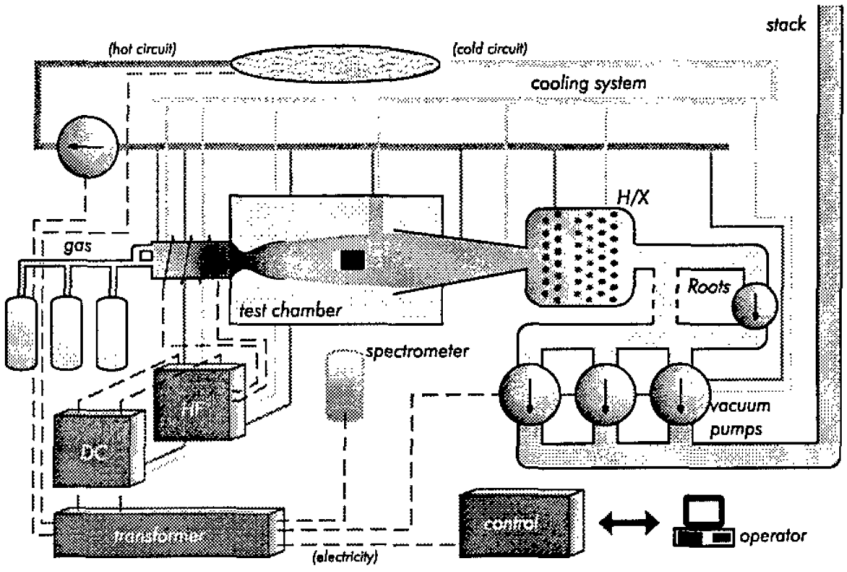

Figure 4.2: Schematic of Plasmatron test facility [Bottin et al. (1999)]

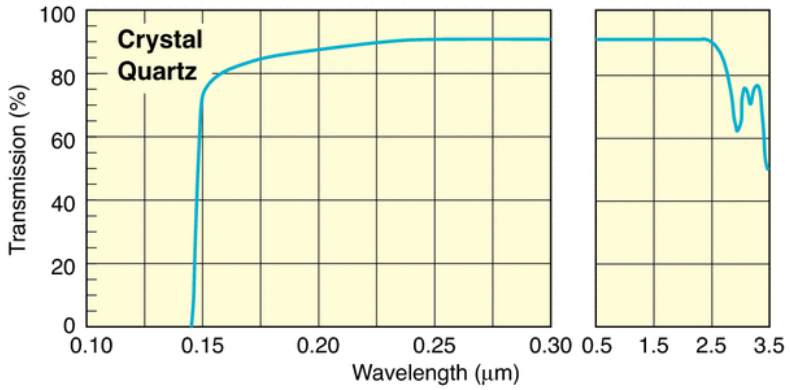

Figure 4.3: Transmittance of optical acess windosws of Plasmatron facility [Newport Corporation (2015)]

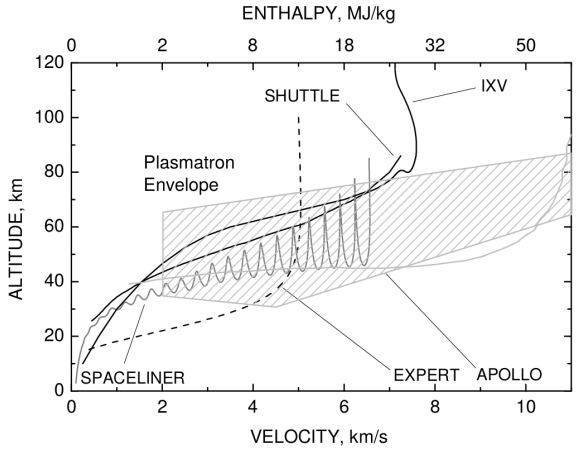

Figure 4.4: Plasmatron operation envelope [Panerai (2012)]

4.2 Measurement Techniques

Ground testing is part of the design and development of new thermal protection systems. It provides insights in the chemical and physical processes that can occur in real flight. For the characterization of ablation a wide variety of measurement methods can be used, the most common techniques are explained in this chapter. Here the measurement techniques used during the project to asses the out-gassing outside of the stagnation region are discussed. The main techniques are optical emission spectroscopy and imaging using a high speed camers, see section 4.2.1. Both these techniques are non-invasive. The third thechnique used during thhis project is the water cooled calorimeter, see section 4.2.2. This techniques is intrusive, so it requires contact with the flow.

4.2.1 Non-invasive Techniques

In this section the non-invasive test techniques are discussed. These techniques main characteristic is that they do not require any contact with the test sample or the flow. To acquire data they only need optical access to the test section, with a clear view on the area of interest. First optical emission spectroscopy is discussed, which is followed by the high speed camera.

Optical Emission Spectroscopy

As described by Bohr, atoms can absorb and emit energy. Take a look at figure 4.5, it shows an atom with two electrons circling the nucleus. Due to some change in the surroundings, the outer electron absorbed some energy (in the form of a photon) and is now rejecting that additional energy (photon) again. By doing so, the electron jumps back to its original orbit and the photon is released into the surroundings. Depending on how many energy levels the electron moved up, the amount of photons it absorbed or the amount of energy the photon(s) contained and the path the electron chooses to take moving back to its original state, the emission of the energy will now have different wavelengths. The choices that each atom can make are specific to the atom, so that each element absorbs and emits photons at unique spectral wavelengths. In case of molecules, the same principle is valid. Each atom in the molecule will emit light at its characteristic wavelengths. Additionally the molecules know vibrational and rotational excitation.

Optical emission spectroscopy is a measurement technique where this emission light of atoms and molecules is observed. Using theoretical and empirical data the measured wavelengths can then be compared and the elements identified. By identifying the elements present around the test sample, the main chemical reactions occurring during hypersonic flight can be deducted, which offers insight in the thermal performance of

thermal protection materials. Usually the atoms or molecules are exited using a laser source, but in case of plasma flows this is not required. Here the atoms and molecules are already exited because of the flow environment. [Broekaert (2005); Pearse and Gaydon (1963); National Institute of Standards and Technology]

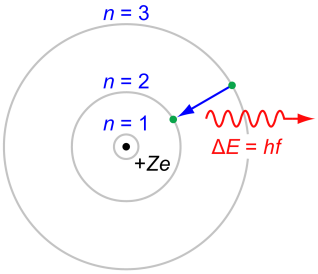

Figure 4.5: Schematic structure od an atom [Bohr (1913)]

Spectrometer Working Principle Figure 4.6 shows the inside of an Ocean Optics USB4000 Spectrometer Ocean Optics (2001-2008), which was used during the project. In the figure each number represents a different component of the spectrometer, their specifics are given in items 1 through 6. Notice that in the figure there are more items than in the list, the items that are not mentioned are optional parts and therefore not necessary for the explanation of the working principle. Table 4.1 lists the Spectroscopic specifications of the spectroscopes used during the project.

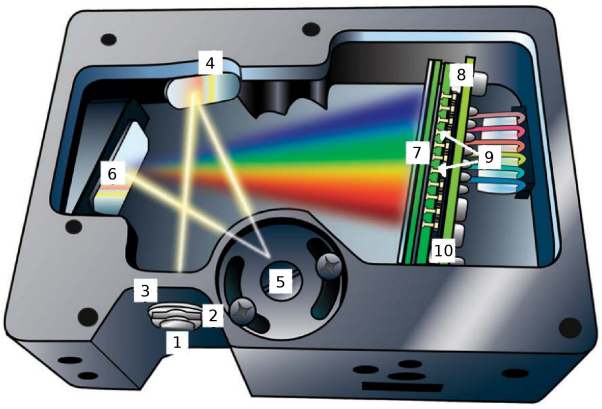

Figure 4.6: USB4000 Spectrometer components [Ocean Optics (2001-2008)]

1. **SMA 905 Connector** secures the optical fiber to the spectrometer and allows the light to enter the spectrometer.
2. **The Slit** is mounted directly behind the SMA Connector. It is a dark piece of material with a rectangular aperture, with a size of 5 μm. The size of the

aperture controls the amount of light that enters the spectrometer and it controls the spectral resolution.

3. **A Filter** is installed to restrict the light radiation to certain wavelength regions before it comes into contact with any of the optics.

4. **Collimating Mirror** After the light has passed through the SMA connector, the slit and the filter it meets the collimating mirror, which focuses the light onto the grating.

5. **The Grating** captures the light from the collimating mirror and diffracts it into the different wavelengths present in the light. The diffracted light is then directed towards the focusing mirror. The groove density of the grating affects the wavelength coverage (200-1200 nm) and resolution of the measurement.

6. **Focusing Mirror** focuses the diffracted light onto the detector plane.

8 **The Detector (UV or VIS)** receives the light from the focusing mirror and converts the optical signal to a digital signal. For every wavelength there is a pixel on the detector. When the light strikes its corresponding pixel a digital response in created. The digital signal of the spectrometer is finally fed into the software application. The UV and VIS indicate that the detector can only identify light in the UV or visible light range (200-1200 nm).

Table 4.1: Spectroscope Specifications [Ocean Optics (2001-2008)]

Wavelength rang	200 - 1200 nm
Integration time	4 ms - 20s (continuous)
Dynamic range	2 10^9 (system)
	2000:1 single acquisition
Signal to noise ratio	300:1
Grating	300 lines per nm grating
Slit	5μm
Optical resolution	0.75 nm FWHM
Stray light	$<$ 5% at 600 nm
	¡0.10% at 435 nm
Buffering	no
Fiber optic connector	SMA 905 to single-strand optical fiber (0.22 NA)

Optical systems The emitted light needs to be fed into the spectrometer, as explained in the list above. Depending on the test set-up this can be achieved using lenses and/or mirrors. For the set-up of the optical path from the measurement location to the inlet of the fiber connected to the spectrometer there is one equation to keep in mind, $\frac{1}{f} = \frac{1}{a} + \frac{1}{f_k}$. In this equation f represents the f-number of the lens, a is the distance from the lens to

the measurement location and f_k is the distance from the lens to the inlet of the fiber. For a focal point measurement, the equation holds as is. If it is wished to measure the light from a larger region (collimated beam), the equation can be discarded. Now the distance between the lens and the fiber inlet (f_k) simply needs to be equal to the lens' focal length.

The use of lenses and mirrors offer an enormous flexibility in the measured region. For a small point measurement the spectrometer will only observe the light locally, while for a larger region, such as a collimated beam, the spectrometer returns the general light impression of the region. A larger region will indicate all the different wavelengths presents in the region but without any information on where these light frequencies are most prominent. A local measurement (focal point) gives a local light response and thus a very accurate impression of the prominent light wavelengths. For this research, it is chosen to use a point measurement so that a local measurement can be made at different locations in the chemical and thermal boundary layer. The comparison of these point measurements can offer insight in the the workings of the species in the boundary layer.

Every material has a spectral transmittance, which indicates which light wavelengths are transmitted through the material. To ensure that the wavelengths of interest do not fall in the opaque zones of the lenses in the set-up, their transmittance curves should be consulted. An example of a transmittance curve of the ThorLabs uncoated UV fused silica 10 mm lens (used during the project) is given in figure 4.7. From this transmittance graph it is known that the lens is transparent over a wide range of wavelengths and opaque for the wavelengths around 1400 nm, 2200 nm and any wavelength larger than 2600 nm. Also towards the high wavelengths, $>$ 1900 nm, the transmittance starts to decline. Knowing from the above list that the spectrometer only detects wavelengths ranging from 200 to 1200 nm, it can be said that there is no problem using these lenses, although the transmittance of the lens also a small decay knows at the low wavelengths, around 200 nm. The optical access window of the test facility has similar properties and thus it is not transparent for all wavelengths. Also for this material the transmittance should be consulted before testing so that one can be sure that the light reaches the spectrometer, see figure 4.3.

Calibration Procedure The spectrometer returns two parameters, the light wavelength and intensity of its signal. Due to the variation in the weather the hardware of the spectrometer needs to be calibrated every couple of months. This wavelength shift on the returned signal is dependent on temperature, air moisture, etc. To correct for this the a measurement should be made using a calibrated mercury lamp. The mercury lamp emits light at discrete wavelengths, of which the theoretical values are well documented. Because the hardware cannot be corrected for the effects of the environment, the signal fed into the software is corrected for the shift in wavelength. The shift is calculated using a third order polynomial describing the relation between pixel number

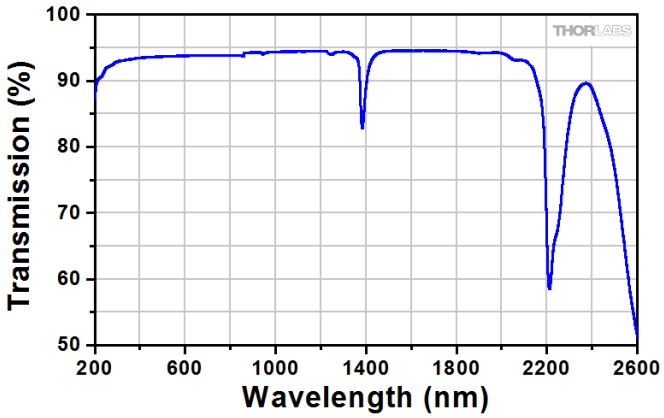

Figure 4.7: Thorlabs uncoated UV fused silica 10 mm lens transmittance curve [ThorLabs Inc.]

and wavelength. The order of this polynomial is predefined by the manufacturer. [Ocean Optics (2001-2008)]

The intensity of the returned signal also needs to be calibrated. Due to small differences between the spectrometers used, their recorded intensities are calibrated to allow an easy comparison between them. This calibration is based on the light emitted from a tungsten ribbon lamp. It is composed of the theoretical response and the normalized measured signal of the tungsten lamp. The normalized signal is the subtraction of the measured and the background signal which is then divided by the integration time. This is the exposed duration of the spectrometer sensor to the light. To obtain the calibration coefficient, a function of the wavelength, the theoretical signal is divided by the normalized signal.

$$C(\lambda) = \frac{S_{theoretical}(\lambda)}{\frac{S_{exp}(\lambda) - S_{exp,BG}(\lambda)}{\tau}} \tag{4.1}$$

In the equation, $C(\lambda)$ is the calibration coefficient as a function of the wavelength, λ. $S_{theoretical}$, S_{exp} and $S_{exp,BG}$ are the theoretical , measured and measured background intensities, all also a function of the wavelength. Finally τ represents the integration time which is the exposure time of the sensor to the light. This calibration should be performed for the different wavelengths at which the experiments will also be conducted or over a range covering the integration times of the tests. Finally the data can be is calibrated by applying equation 4.2. Now τ should be set to the integration time of the

test and $S_{exp,calibrated}(\lambda)$ describes the calibrated signal.

$$S_{exp,calibrated}(\lambda) = \frac{S_{exp}(\lambda) - S_{exp,BG}(\lambda)}{\tau} C(\lambda) \tag{4.2}$$

High Speed Camera

At the VKI, a Vision Research Phantom 7.1 CMOS high speed camera is used to observe tests at high sampling frequency, but with low resolution. The camera uses a exposure time of only 2μ sec to achieve a time-lapse video of the test, the exposure time is low to avoid the digital sensor from being damaged by the high intensity of the emitted light. The resolution of the frames is directly related to the accuracy of the recession measurement, the uncertainty is about $0.2mm$. For an accurate recession measurement it is important to have a sharp surface edge in the frames. The movement of the surface edge is measured over time which results in the recession rate. The sharper the edge the more accurate the movement of this edge. The camera resolution defines how many pixels there are in each of the frames, so to have sharp edges the resolution should be high, which corresponds with a high amount of pixels. The camera specifications are given in table 4.2 and a test set-up image is shown in figure 4.8. During the test, the high speed camera is installed with a UV-lens and a UV-filter, the specifications for these parts is given in table 4.3 and the filter transmittance is given in figure 4.9.

Table 4.2: High speed camera specifications

Sensor size [pixel]	800 × 600
Sensitivity	4800 ISO/ASA monochrome
Picture per Second [pps]	
full sensor	4 800
frame 512 × 384 pixels	10 000

Calibration Procedure The alignment of the camera with the test sample is an important concern in the set-up. If the camera observes the sample from a skewed angle, the measurements will be influenced by this and can possibly corrupt them. The alignment with the naked eye is limited in accuracy, therefore a calibration is performed. With this calibration the frames are corrected afterwards for any small error in the alignment, this includes rotational and translational misalignments.

For the calibration, pictures are taken with the camera placed in its final position, afterwards it is also vital that the camera remains in that position during the entire duration of the testing, if not the calibration has to be redone. Pictures of a checkerboard

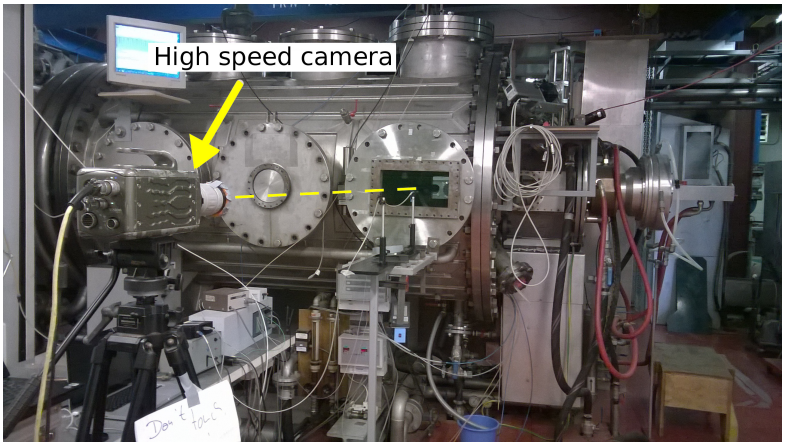

Figure 4.8: High speed camera test set-up

Table 4.3: Filter and Lens specifications [Semrock]

Filter Specifications	
Filter Name	380/14 nm BrightLine single-band bandpass filter
Transmission Band	373-387 nm
Center Wavelength	380 nm
Diameter	25 mm
Mounten Thickness	5 mm
Lens Specifications	
Lens Name	100 F/2.8 type CERCO 2178
Focal Length	98 mm
F stop	F/2.8-F/8
Manual Focus	∞ - 45 cm
Field of view	14.5 °
Picture size	25 mm
Spectral Range	250-410 nm
Transmission in UV-range	90% inside spectral range
Materials	Synthetic fused silica and UV grade mono-crystal calcium fluoride
Length	97-121 mm
Outside Diameter	66 mm

from different angles are taken with the camera. Because the camera has to remain stationary and the limited space in the test section, the different angles are obtained by simply tilting the checkerboard in the test section at the location where the test sample would be during testing. From the different perspectives in the pictures, the location of the camera with respect to the test sample location is obtained. This is done using a build in Matlab® function. This function identifies the crossings of the checkerboard

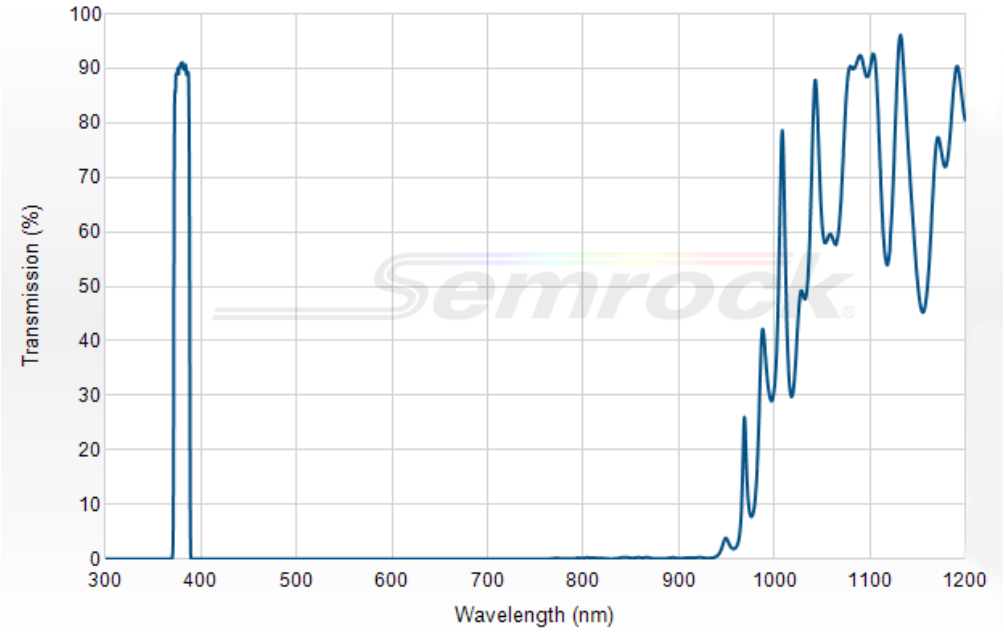

Figure 4.9: Filter transmittance (Semrock)

squares in the board and choses one of them as the origin. Based on the different angles of the perspectives, the orientation of the camera with respect of the test sample is determined.

Because during the initial alignment, the frame is positioned such that the sample is placed in the center of the frame with a clear space around it such that also the gas around the sample can be observed. The rotational alignment is the most important. The results of the calibration are finally using to correct the perspective of the frames.

4.2.2 Invasive Techniques: Water Cooled Calorimeter

A water cooled calorimeter, allows the user to measure the heat flux of the plasma jet. The Von Kármán institute calorimeter consists of a copper plate mounted on a probe so that it has a similar geometry to the test sample. The copper plate is pre-oxidized to avoid chemical reactions to corrupt the measurement, see figure 4.10. The shape and size influence the velocity gradient in the boundary layer which is important for the chemistry occurring in the boundary layer. From section 2 it is known that the high temperature region consists of the entire boundary layer which is also the shock layer. By using a different probe geometry, the shock wave shape and thus the high temperature region is altered. This can be corrected through geometrical mapping. [Zoby and Sullivan (1966)] The stagnation region is isolated from the rest of the probe so that adiabatic conditions are obtained at the wall. The insulation of the stagnation point from the rest of the probe is done to avoid any outside influences to corrupt the measurement, such as side wall heating. It is chosen to measure the heat flux in this region, as this region encounters the highest heat fluxes. The adiabatic wall condition is obtained by insulating the calorimeter from the probe holder using a Teflon insulator.

The cooling circuit of the calorimeter is an independent system, which allows the flow rate and temperature of the water to be measured using a calibrated rotameter and two thermocouples, one for the incoming and one for the outgoing flow. They measure the mass flow rate and temperatures. Finally the heat flux of the plasma jet is obtained from the temperature difference and mass flow of the water going into the system and the water coming out of the system. A schematic of the calorimeter is given in figure 4.10, the temperature at the stagnation point is calculated according to equation 4.3, where q is the convection energy, S the area of the measurement area, $\dot{m}$ the mass flow, c_p the specific heat of the water in the system and T is the temperature of the water flowing in and out of the system, indicated with subscripts *in* and *out* respectively. (**?**)

$$qS = \dot{m}c_p(T_{out} - T_{in}) \tag{4.3}$$

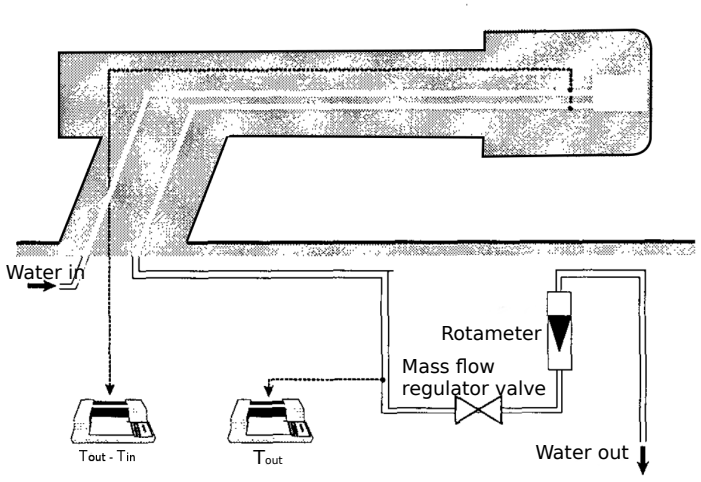

Figure 4.10: Calorimeter schematic (?)

Chapter 5

Boundary Layer Characterization

Lets look at figure 5.1, it shows a clear bright flame around the test sample. The test sample in this figure is subjected to a heat flux of 3 MW/m^2 in an air plasma jet at 200 mbar pressure. Due to the high pressure and the high heat flux small soot particles from the pyrolysis process were released by the test sample and have entered the flow where they oxidize (burn). The presence of the flame is not something that always occurs. If the material is subjected to test conditions (heat flux and pressure) high enough to force some larger pieces of material to erode, the flame can occur in air plasma. From the image it can be seen that for this test at this moment in time, the white flame is only present at the side of the test sample, while the red flame goes around the entire test sample. From the geometries of the flames it can be seen that there are no soot particles originating at the stagnation point region at this time instant, but there are still particles originating from the sides.

In this chapter a first attempt is made to observe which species govern the flow in the side-wall region, where in the boundary layer are these species more dominant and when are they strongest. Using three spectrometers placed in a vertical row below the test sample, a spatial comparison can be made between the spectrometers related to their respective distance from the surface. This allows us to identify the different species in the chemical and thermal boundary layer. From literature [Helber et al. (2014)] it is known that in the stagnation point region the strongest radiators are CN violet and C_2 Swan. The first, CN violet, is a product of pyrolysis and ablation, while the second, C_2 is only a product of pyrolysis. Because spectrometers allow multiple measurements to be made during testing, they also offer a temporal response of each of their respective measurements. When the intensity of the main species identified are plotted over time, it can be said if they are produced during ablation or pyrolysis. For a pyrolysis product, initially there will be peak, which will then decrease. As explained in section 3.1.1,

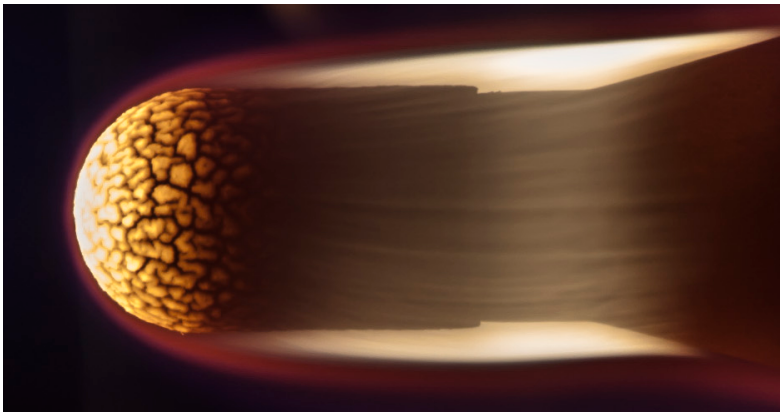

Figure 5.1: Example of test with visible flame (Cork test sample with a 15 mm radius, air plasma, 3 MW/m^2, 200 mbar)

initially there is a pressure build up in the test sample as the organic resin in the material evaporates, this increase in pressure causes the created gases to burst out of the material. As time progresses there is less virgin material producing pyrolysis gases and thus the pressure with which these leave the material also decreases. Ablation on the other hand is a quite steady process.

In section 5.1 the test set-up is explained together with the measurement technique, spectroscopy and the test matrix of this part of the project. The measurements made at this time were conducted as part of the research of I. Sakraker. Therefore it is chosen to keep the test names as they were appointed by her. Finally section 5.2 gives the results of the measurements, first the spatial response is elaborated, followed by the temporal response and last the effect of the visible flames, such as in figure 5.1.

The material used during the testing was the material of the P50 thermal protection system, which is made from cork granules, which was processed into sphere-cylinder shaped test samples. [Amorim (2013)] Cork has the natural ability to be very resistant to fire. Just like ablative thermal protection materials, it contains organic resin (phenolic) that will evaporate when the surrounding temperature increases too much (pyrolysis). Next when the resin is completely gone, the carbon left will burn as the heat continues (ablation). For the tree this particular characteristic allow it too survive forest fires while other plants will not, giving it an advantage. The main purpose of the cork (bark of the tree) is the same as the ablative thermal protection material.

5.1 Test Set-up and Measurement Technique

To scan the boundary layer developing around the test sample it was chosen to use emission spectrometers as these are able to scan a wide range of wavelengths, are easy to set-up, calibrate and use. Figure 5.2 shows a scheme of the test set-up from a side and front perspective. From figure 5.2(a) it can be seen that the three spectrometers are used. The spectrometers are vertically aligned and measure the emission in their focal points. The specifics of the spectrometers can be found in section 4.2.1.

In figure 5.2(b) it is shown that the spectrometers obtain optical access to the test chamber through a window in the plasmatron wall. As already previously stated, the window allows the measurement devices to see in the UV-light range and in the ultra violet range. The specifications of the plasmatron can be found in section 4.1. The specifications of the spectrometers is given section 4.2.

In the test matrix, table 5.1, not only the test conditions are given, but also the measurement settings for the spectrometers are presented. In this table, the integration time refers to the duration of the measurement, the acquisition frequency defines when each measurement is triggered. The gas used to create the plasma is not mentioned in the matrix as it was the same for all tests, namely air. The spectrometers were assigned a name so that their location with respect to the surface could easily be derived, C stands for the spectrometer closest to the surface, M for the middle and F for the furthest.

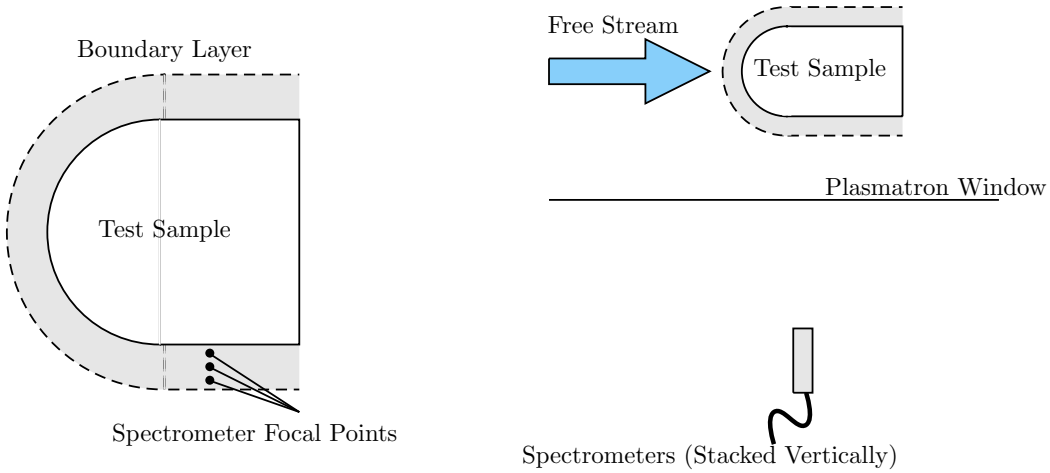

(a) Side view (b) Top view

Figure 5.2: Schematic representation of the measurement

Table 5.1: Test Matrix: Campaign one

Test number	Sample Radius mm	Heat Flux MW/m^2	Pressure mbar	Duration sec
26	15	3	200	13
15	15	1	15	37
21	15	0.28	41	170
18	15	3	15	17
22	11	0.28	41	120
9 repetition	25	1	15	48
	Integration Time			Acquisition Frequency
	C [ms]	M [ms]	F [ms]	Hz
26	20	20	10	2.5
15	100	100	100	1
21	150	150	75	1
18	20	20	10	1
22	200	200	200	1
9 repetition	200	200	200	2

5.2 Discussion of the Test Results

To make sense of the amount of data collected during this test campaign, the results are split up into three. First the spatial measurements are discussed in section 5.2.1, this will be done in two observations. The first is to see what the effect of the spectrometer distance to the surface is on the measurement and secondly the the influence of the test sample size on the measurement is observed. The second part of the test results is to observe how the species evolve over time, section 5.2.1. Finally the presence of the flames in some of the tests is discussed. As mentioned in section 3.4 with this test campaign it is aimed to get an idea of which species are most important in the side wall region. Due to the large amount of data collected during this testing only a selection of the tests is presented here. The complete test matrix is given in appendix A.

5.2.1 Spatial Measurement

Lets consider tests 26, 21, and 15, their test conditions were given in table 5.1. The spectral measurements of these tests at 1 second, 5 seconds and 10 seconds after injections can be found in figures 5.3 to 5.5, 5.9 to 5.11 and 5.6 to 5.8, respectively. Together these tests span all the heat fluxes and pressures that were used during the test campaign. These three tests have the same sample size so that the effect of the size on the boundary layer cannot influence the conclusions.

To see if the size of the sample plays an important role in the presence of species in the flow, one additional test is presented, test 22. Also the test conditions for this test were given in table 5.1. Test 22 shares the exact same test settings with test 21, but its sample size is smaller. The spectral measurement figure for test 22 is given in figures 5.13 through 5.15.

Influence of the distance to the sample surface

Three tests have been selected to observe the effect of the distance to the surface. The tests are test 26, 21 and 15. The test conditions for these can be found in table 5.1. Together these tests span both high and low heat flux and pressure test conditions. This can indicate that the material responds differently under different conditions and what material reactions remain constant throughout different test conditions.

High heat flux and pressure First lets look at figures 5.3 to 5.5, these represent the spectral response of test 26 (15 mm radius, 3 MW/m^2, 200 mbar) after being injected for about 1 second, 5 and 10 seconds. The first thing that stands out looking at figure 5.3 is that intensity of the spectra decreases as the distance from the spectrometer to the surface increases. This is an expected result as the species originate from the test sample. The species present in the measurement are CN violet, C_2 Swan and potassium, it is expected that CN violet is very prominent in the flow due to the high pressure. The high pressure implies that there is a lot of air in the test section and thus also a lot of nitrogen for the carbon, created by pyrolysis, to combine with. The C_2 Swan is known to be an pyrolysis product, which is only present in the measurement closest to the surface, indicating that there is only a small amount of C_2 Swan produced. The potassium measurement can be caused by an impurity in the material or on the surface of the test sample. Any salts, potassium or sodium, present in emission measurements are considered to be noise since the salt could have been transfered into or onto the material at any time. The furthest spectrum also measured CN violet, potassium and sodium but the signal is very weak indicating that this is the edge or end of the boundary layer. Finally the spectra show a curve, these are Planck curves. Planck curves are measured by spectrometers as they observe the light emitted by solid objects. This implies that there is a solid object in front of the spectrometer, which leads to the conclusion that there are soot particles in the flow and that there is a flame around the test sample such as in figure 5.1. The effect of flames in the boundary layer and the measurements is explained in section 5.2.3.

5 seconds after injection (figure 5.4), not a lot has changed. The Planck curves are now only present in the measurement made by the middle spectrometer indicating that the flame is dying out. Also C_2 Swan has disappeared from the measurements and CN violet has gained intensity in the measurement of the closest spectrometer. Due to the high pressure it could occur that all the carbon released by the test sample are combining

with other elements in the flow, such as nitrogen, rather than combining with itself. Finally after 10 seconds (figure 5.5), the intensity of all species start to decrease, which can be appointed to the consumption of the material. Also notice that the intensities first increase before they decrease with time. It is expected that the species' intensities decrease over time due to the consumption of the test sample, and thus the decrease in material to be consumed by the plasma flow. The initial increase however is unexpected. A more detailed assessment of the influence of time on the intensity of the species is given in section 5.2.2.

Low pressure Next let us take a look at test 15 (figures 5.6 through 5.8, which was performed at a heat flux of 1MW/m^2 and a pressure of 15 mbar. Due to the lower heat flux there is less heat convection to the surface, which causes pyrolysis to occur at a slower pace than at a heat flux of 3 MW/m^2 and the excitation of the species in the flow will be less than for higher heat fluxes. This will cause the intensities of the measurements to be lower. The main difference between the two tests is the large difference in the pressure. A low pressure translates to few species for the pyrolysis or ablation products to react with, such as the oxygen and nitrogen of the free stream. Therefore C_2 Swan is more present compared to the previous test. The overall decrease of the intensity of the measurements with the distance from the surface is consistent with the previous test. The intensity also deceases over time as observed in these test results as in the results of the previous test, which is cause by the consumption of the test samples.

Low heat flux Finally the influence of a low heat flux is observed. Test 21 is performed with a 0.28 MW/m^2 heat flux and 41 mbar pressure. This means that there is an increase in the amount of species in the free stream, but their excitation is drastically lowered. As can be seen in figures 5.9 through 5.11. Indeed, the intensity of the measurements has decreased significantly, in these measurements the strongest radiator is sodium. Even though the species have low intensities, they are still present. For this test there is both CN violet and C_2 Swan present in the flow over the entire course of the test. This cam be assigned to the 41 mbar pressure, which is low enough for both of the species to appear.

From these it can be concluded that the pressure mostly influences which species are created during the test and the heat flux influences there state of excitation. Also In each of the tests, independent of there conditions the intensity of the measurement decreased with the distance to the surface. How the species evolve over time is still unclear, therefore this will be discussed separately in section 5.2.2. Next the influence of the test sample radius on the boundary layer species is investigated.

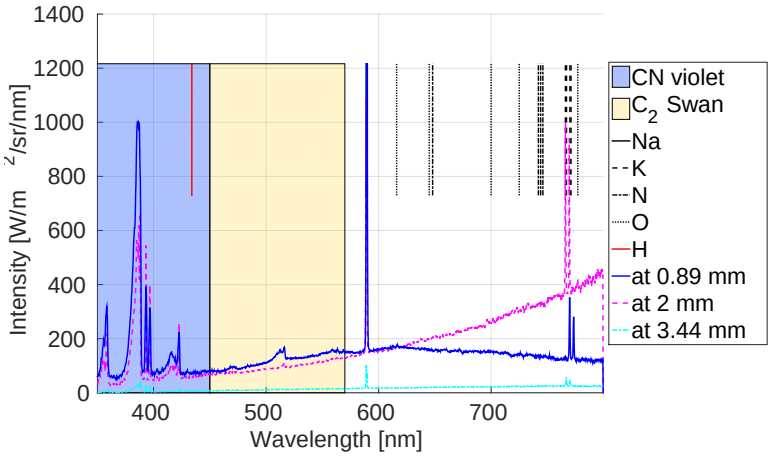

Figure 5.3: Test 26: 1 second after injection (Air, 15 mm radius, 3 MW/m^2, 200 mbar)

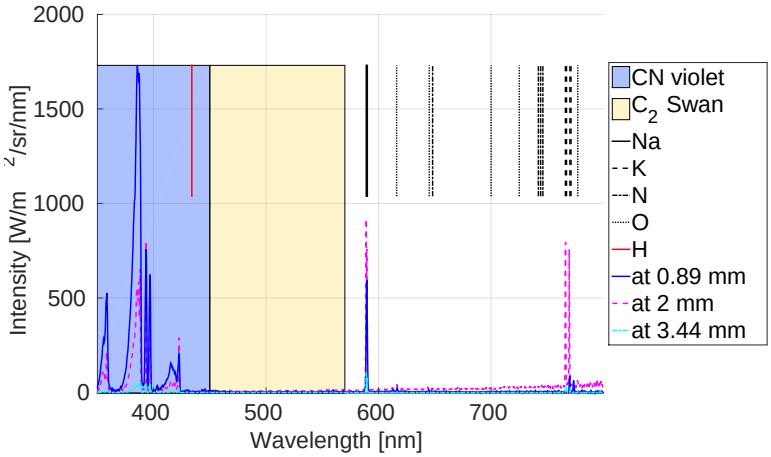

Figure 5.4: Test 26: 5 seconds after injection (Air, 15 mm radius, 3 MW/m^2, 200 mbar)

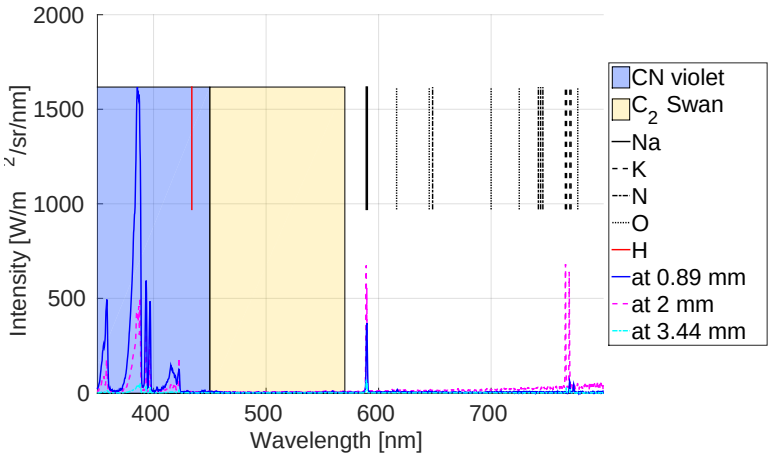

Figure 5.5: Test 26: 10 seconds after injection (Air, 15 mm radius, 3 MW/m^2, 200 mbar)

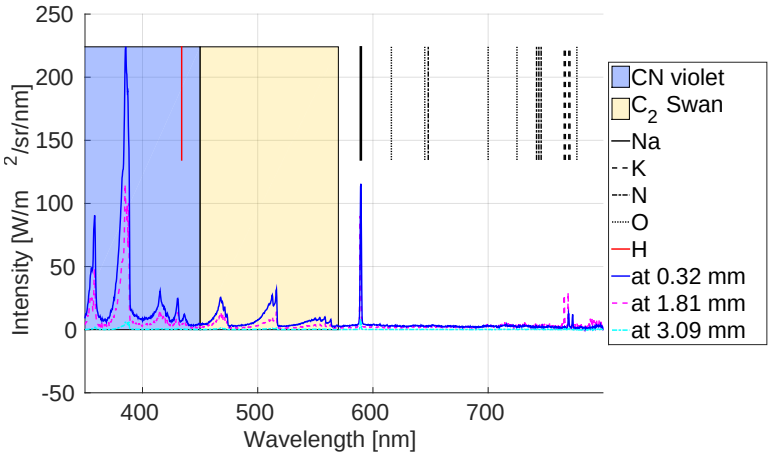

Figure 5.6: Test 15: 1 second after injection (Air, 15 mm radius, 1 MW/m^2, 15 mbar)

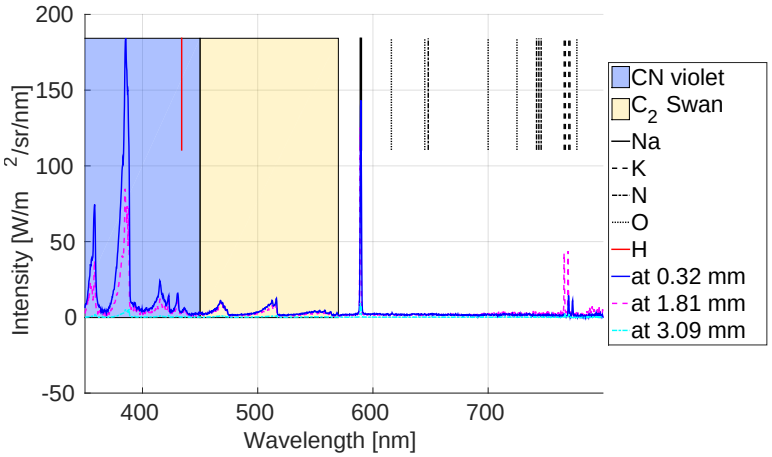

Figure 5.7: Test 15: 5 seconds after injection (Air, 15 mm radius, 1 MW/m^2, 15 mbar)

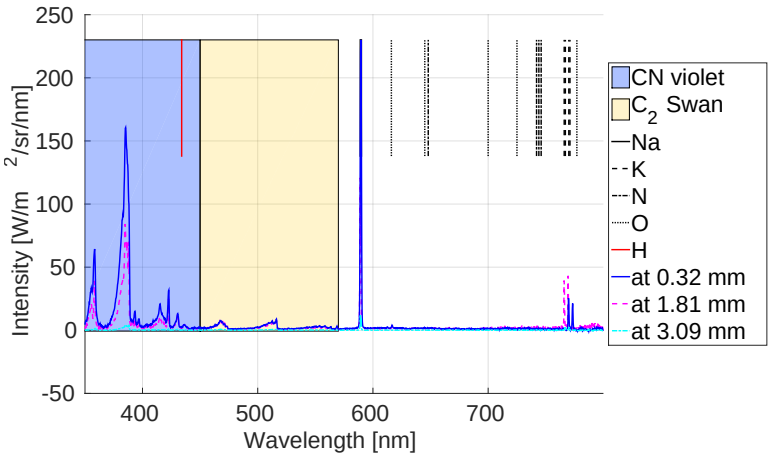

Figure 5.8: Test 15: 10 seconds after injection (Air, 15 mm radius, 1 MW/m^2, 15 mbar)

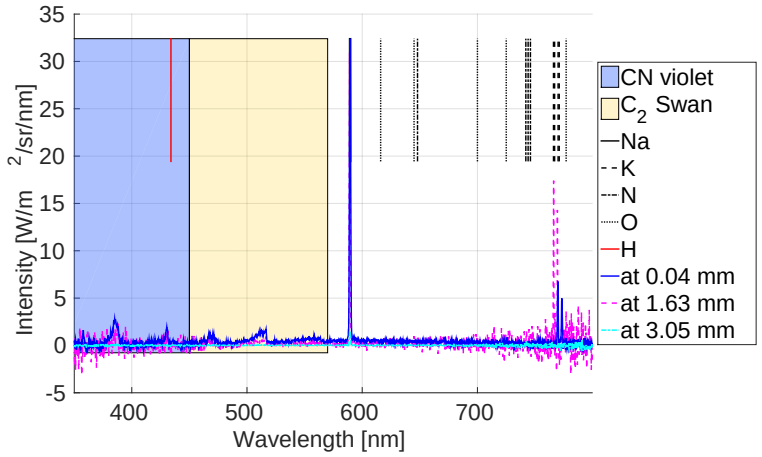

Figure 5.9: Test 21: 1 second after injection (Air, 15 mm radius, 0.28 MW/m^2, 41 mbar)

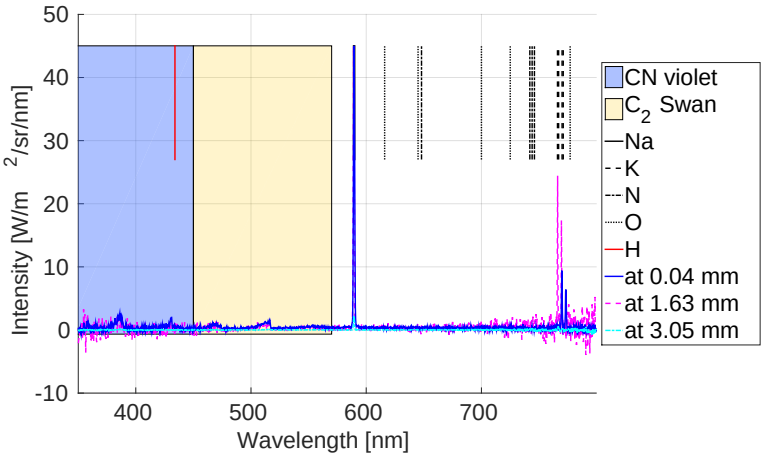

Figure 5.10: Test 21: 5 seconds after injection (Air, 15 mm radius, 0.28 MW/m^2, 41 mbar)

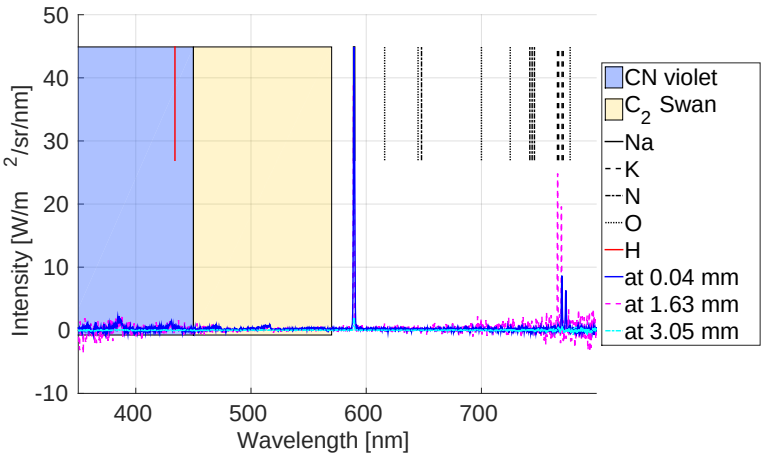

Figure 5.11: Test 21: 10 seconds after injection (Air, 15 mm radius, 0.28 MW/m^2, 41 mbar)

Influence of the test sample size

For this comparison test 21 and 22 are compared, the test sample radius is test 22 is smaller (11 mm) than the radius of test 21 (15 mm). The differences in sample radius are not the only differences that can influence the measurement, the location of the spectrometer focal points are not exactly the same for each test. This can be seen in table 5.2 where the distances of the spectrometer focal points are given for tests 21 and 22, the definition of the distances are presented in figure 5.12. The x-direction is defined to originate in the stagnation point and continue along the test sample's symmetry axis, the y-direction also originates in the stagnation point but continues down tangentially to the test sample surface in the stagnation point.

From Zoby and Sullivan (1966) it is known that the geometry of the test sample plays a major role in the magnitude of the flow velocities close to the surface, which can influence the chemistry close to the surface. As a general rule it can be stated that the smaller the test sample the closer the chemical processes occur to the surface which could increase the excitation of the species.

The measured spectra of test 22, 5 seconds after injection, are presented in figures 5.13 through 5.15. Each figure shows the spectra measured with the same spectrometer for both tests. It is chosen to present the spectra like this so that the differences between the measurements can be observed in detail. The tests are performed under the same test conditions, 0.28 MW/m^2 heat flux and 41 mbar pressure, but the sample radius is 11 mm for test 22 and 15 mm for test 21. At first sight the spectra of both test look very similar, which is expected as they are subjected to the same environments. But a closer look shows that the spectra of test 22 registered a slightly higher intensity. This is especially clear in figure 5.14. As explained above a smaller test sample would lead to a compression of the reactions and the species closer to the surface, and thus an increase in the measured intensity, which is what is seen in the figures. From the above comparison on the influence of the distance from the surface, it is known that the intensity will decrease with distance from the surface. According to this the spectra of test 22 should have a lower intensity for test 22, see table 5.2. This is not visible in the figures. Finally if the boundary layer for test 22 is thinner than for test 21, then it could be that the furthest spectrometer of test 22 does no longer observe the boundary layer, since it is located far away from the surface, see figure 5.15. Unfortunately neither of the two tests show many species in at this location. So it can only be concluded that indeed the smaller radius leads to an increase in species excitation.

Table 5.2: Focal point distances of test 21 and 22, given in millimeters

	Test 21		Test 22	
	x-distance	y-distance to surface	x-distance	y-distance to surface
Closest to the surface	23.27	0.04	29.57	0.26
Middle point from the surface	23.34	1.63	29.59	2.29
Furthest from the surface	23.38	3.05	29.64	4.21

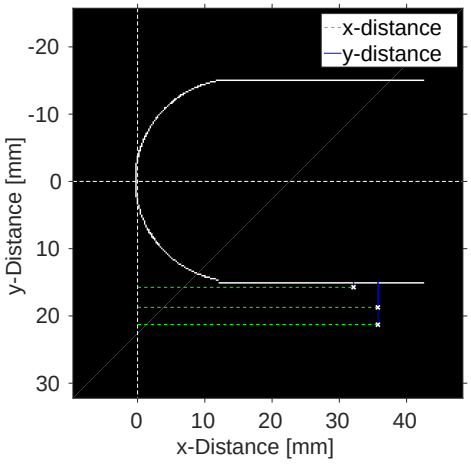

Figure 5.12: Schematic representation of the defined distance to the surface

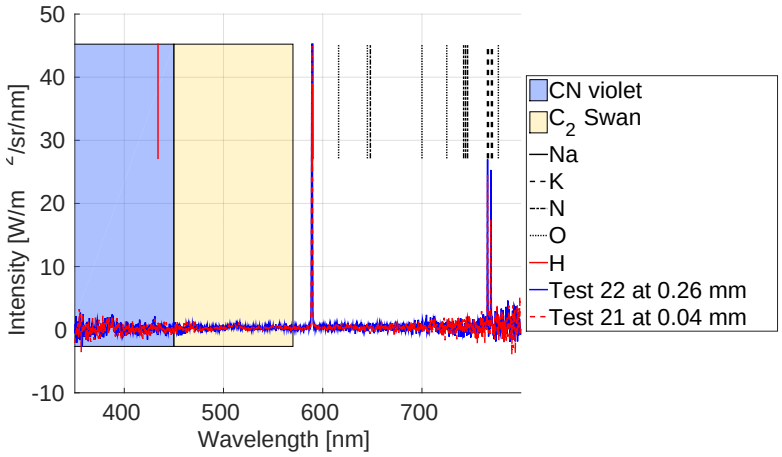

Figure 5.13: Test 22 and 21: 5 seconds after injection (Air, 11 mm radius, 0.28 MW/m^2, 41 mbar)

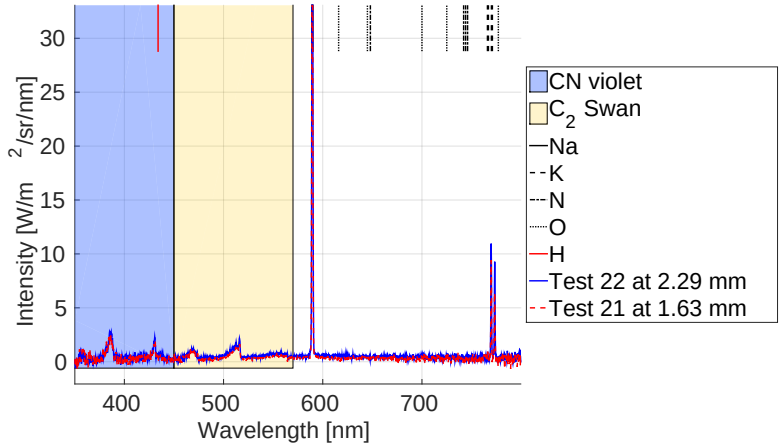

Figure 5.14: Test 22 and 21: 5 seconds after injection (Air, 11 mm radius, 0.28 MW/m^2, 41 mbar)

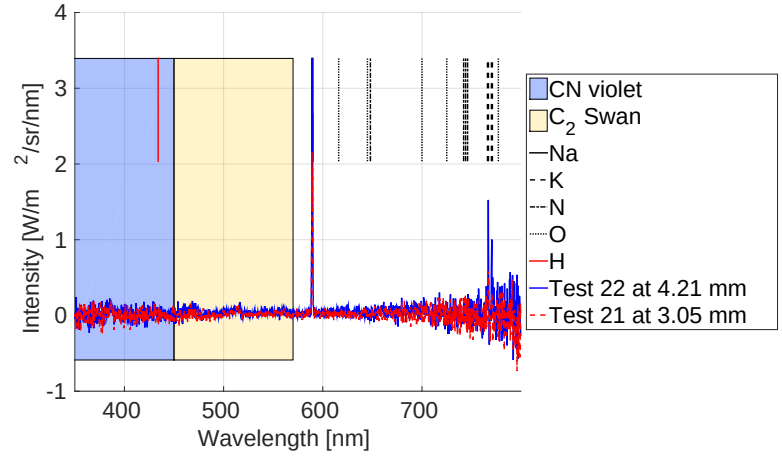

Figure 5.15: Test 22 and 21: 5 seconds after injection (Air, 11 mm radius, 0.28 MW/m^2, 41 mbar)

5.2.2 Temporal Measurement

Apart from the spatial response, the species can be followed during the test and give information on the effect of time. In this section only C_2 swan and CN violet are used to investigate the temporal response. First compare some tests with each a different heat flux, test 26, 15 and 21, their test conditions can be found in table 5.1. In figures 5.16, 5.18 and 5.20 the evolution of CN violet is given for the three chosen tests, respectively. Similarly, figures 5.17, 5.19 and 5.21 are presenting what happens with C_2 swan over time. In the graphs the beginning of the measurement is indicated with the zero on the x-axis. The injection of the test sample can be seen from the sudden initial peak in the curve. In the graphs the species are represented with a single line, even though they are actually a system of different wavelengths. Therefore the wavelength which was largest five seconds after injection was chosen. The intensity value of this wavelength was then plotted over time.

First look at each image individually, according to test 26 and 15 indeed the intensity decreases with distance to the surface. For test 21 this is not true, the intensity of CN violet is highest at 2 mm distance. It is suspected that 0.04 mm from the surface is not far enough for most of the carbon atoms to combine with the free stream nitrogen. Next compare the development of CN violet and C_2 Swan. In all tests, C_2 Swan decays to zero while CN violet approaches a constant value. This is due to the origin of the species production. C_2 Swan is a purely pyrolysis product and as explained in section 3 the amount of atoms created due to pyrolysis reduce over time. CN violet on the other hand is formed by both processes. At first, when pyrolysis is strong the CN violet knows a great peak. Next as pyrolysis proceeds and decreases in strength, the intensity on CN violet gradually reduces. At some point ablation becomes the dominant process, which progresses at a more steady rate, causing the CN violet species to be formed at a constant rate and the intensity to stagnate. For test 15 this is not true, C_2 Swan does not decay to zero, which can only lead to the idea that the test was ended before the pyrolysis could die out. From the CN violet graph, figure 5.18, it can be seen that the test was ended after about 25 seconds, due to the sudden drop in all intensities. At this point in the C_2 Swan curve, figure 5.19 did not decay to zero yet. This means that there was still virgin material in the test sample at the end of the test.

Finally the response between the different tests is observed. Test 26 (3 MW/m^2, 200 mbar) experiences a brutal injection peak that knows a great fall almost immediately after. Test 15 (1 MW/m^2, 15 mbar) on the other hand knows a weaker initial peak and a more gradual and longer decay. Finally, test 21 (0.28 MW/m^2, 41 mbar) does not seem to experience a high initial peak or a steady decay. Due to the extreme heat flux of test 26 the pyrolysis occurs very fast and powerful, as the heat flux is reduced (test 15) this initial peak decreases and pyrolysis is prolonged. If the heat flux is reduced to a very small magnitude (test 21), the temperature does not increase enough for pyrolysis to occur.

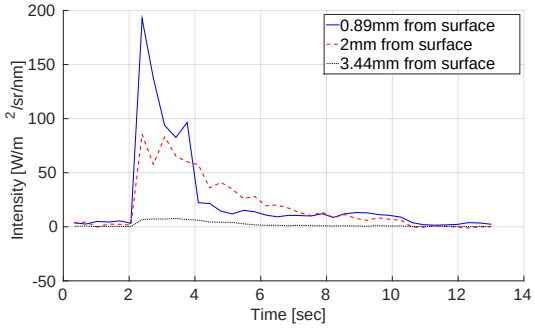

Figure 5.16: Test 26: CN violet with respect to time (Air, 15 mm radius, 3 MW/m^2, 200 mbar)

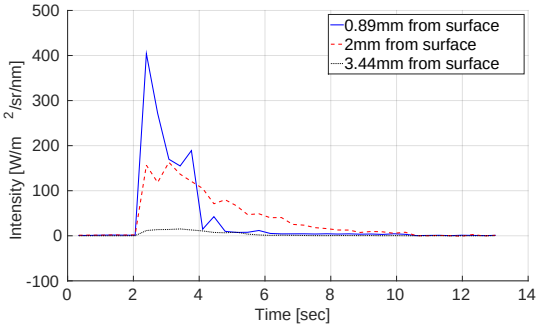

Figure 5.17: Test 26: C_2 swan with respect to time (Air, 15 mm radius, 3 MW/m^2, 200 mbar)

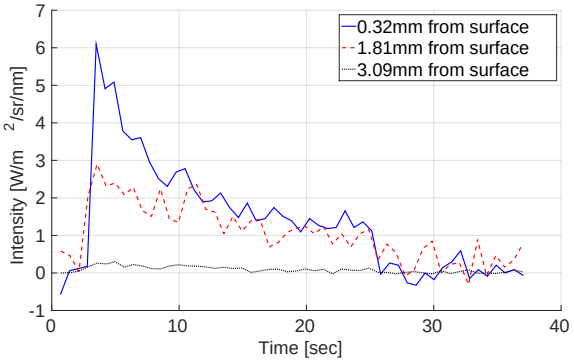

Figure 5.18: Test 15: CN violet with respect to time (Air, 15 mm radius, 1 MW/m^2, 15 mbar)

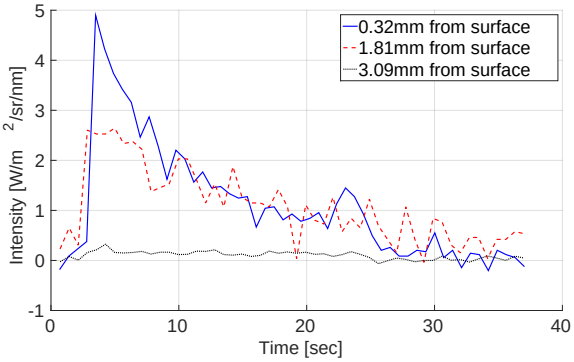

Figure 5.19: Test 15: C_2 swan with respect to time (Air, 15 mm radius, 1 MW/m^2, 15 mbar)

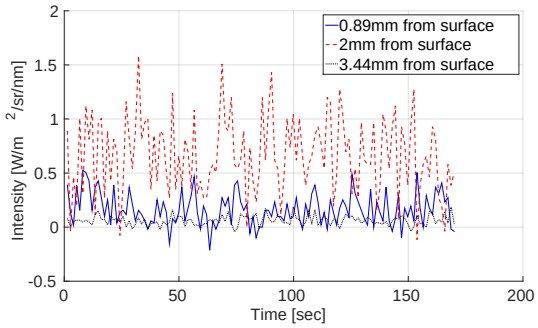

Figure 5.20: Test 21: CN violet with respect to time (Air, 15 mm radius, 0.28 MW/m^2, 41 mbar)

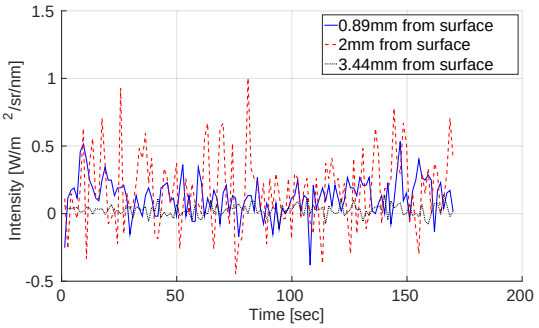

Figure 5.21: Test 21: C_2 violet with respect to time (Air, 15 mm radius, 0.28 MW/m^2, 41 mbar)

5.2.3 The Effect of Flames on Intensity

During the test campaign each test was observed with a reflex camera, this allows the test to be reviewed afterwards. It was noticed that test 26 shows a Planck curve. Figure 5.22 shows the test after about 4 seconds. The figure shows a bright white flame with a small red flame at the edge of the white flame. The observed spectra belonging to this instant in time are given in figures 5.23 to 5.25.

As is known a Planck curve represents the radiation of a hot surface. In this case the bright white light does not originate from a body. As the test sample is subjected to the test conditions, it can occur that small soot particles are released from the surface before they are reduced to atoms. When this occurs the particles oxidize in the free stream causing a glow to appear. This is what happened here. Because the spectrometers were directly pointed into the flame it is probable that the material causing this is was observed.

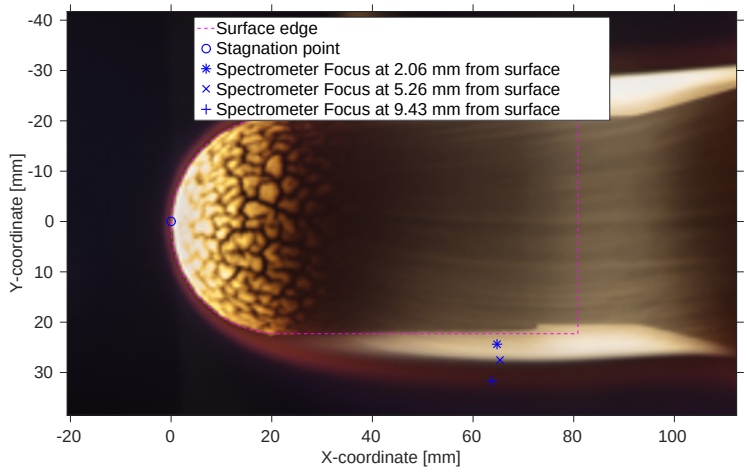

Figure 5.22: Test 26: Test snapshot 4 seconds after injection (Air, 15 mm radius, 3 MW/m^2, 200 mbar)

As expected a Planck curve is visible in every spectrum graph. The peak of the Planck curve is focused at the emission wavelength of sodium, which is also the wavelength range of yellow light and ranges over almost the entire visible spectrum of light. This could explain the whiteness of the flame. Another strong radiator in this spectrum is CN violet, which corresponds to the violet and blue visible light. This might explain the blue/red edge in the flame.

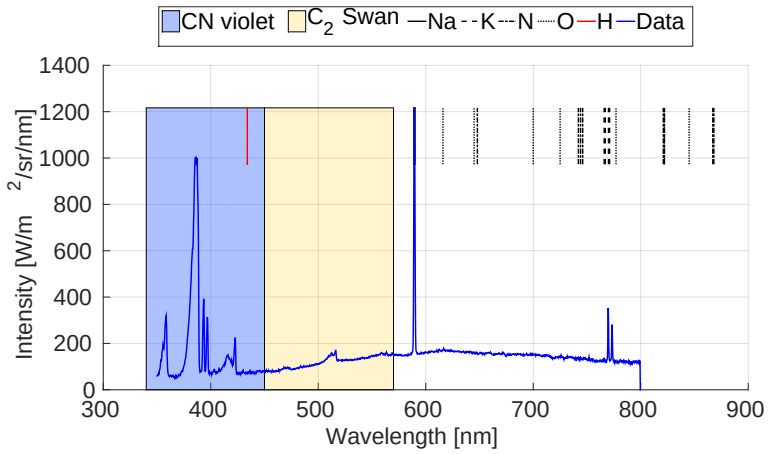

Figure 5.23: Test 26: Spectrum graph 0.89 mm from the surface, 4 seconds after injection (Air, 15 mm radius, 3 MW/m^2, 200 mbar)

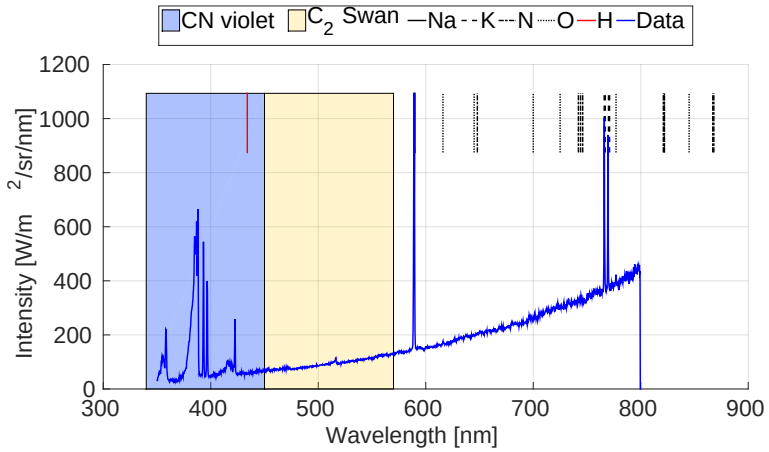

Figure 5.24: Test 26: Spectrum graph 2.00 mm from the surface, 4 seconds after injection (Air, 15 mm radius, 3 MW/m^2, 200 mbar)

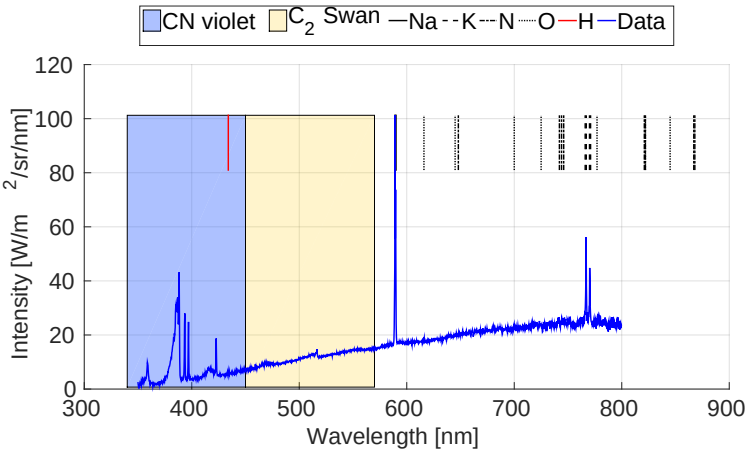

Figure 5.25: Test 26: Spectrum graph 3.44 mm from the surface, 4 seconds after injection (Air, 15 mm radius, 3 MW/m^2, 200 mbar)

Chapter 6

Imaging CN violet in the Boundary Layer

As explained in section 5.2.1, one of the main radiators in the boundary layer is CN violet. The presence of this specie can have two reasons, it can be a product of pyrolysis or nitridation of the surface after pyrolysis (Helber et al. (2014)). To investigate this difference, some tests are performed using graphite and cork test samples. As the graphite test sample does not contain anything else than carbon (C) and cannot pyrolyze, it is sure that the CN violet in the boundary layer from the graphite sample is due to the nitridation (N) of the surface, C + N $\rightarrow$ CN. Cork on the contrary contains a lot of phenolic resin, so that the CN violet in the boundary layer can belong both to the pyrolysis of the resin as to nitridation of the surface. Considering that the discussion in this chapter deals with the formation of CN violet, the boundary layer in the text refers to the thermal and chemical boundary layer around the test sample.

6.1 Test Set-up and Measurement Technique

The testing of the CN violet in the boundary layer is performed in the VKI plasmatron, see section 4.1. The test samples used to study the presence of CN violet in the boundary layer have a diameter of 50 mm and are made out of cork or graphite. In this part of the study two things are of interest, the comparison of the boundary layer of the graphite sample with and without UV-filter and the comparison of the cork and graphite boundary layer.

The CN violet around the test sample is imaged using a high speed camera, UV-lens and a bandpass filter in the UV-light spectrum. The specifications can be found in section 4.2. The UV-lens allows the CN violet to be observed by the camera as its wavelengths

are in the UV-spectrum. Using the lens in combination with the filter makes the camera only observe the light emitted by CN violet. It was chosen to image the test using a high speed camera rather than using a spectrometer again, because now the entire test sample and chemical and thermal boundary layer are recorded rather than three individual points. A schematic of the test set-up is given in figure 6.1 and the test matrix is given in table 6.1. First the two graphite tests, test 1 and 2, are compared to see if the filter blocks a lot of light or if the boundary layer mostly consists of CN violet. Second the graphite test with filter, test 2, is compared to the cork test, test 3, to investigate the difference between a pyrolyzing and not pyrolyzing material. As in the previous chapter, the plasma gas is not given in the test matrix, because it is the same for all three tests. They were tested in air.

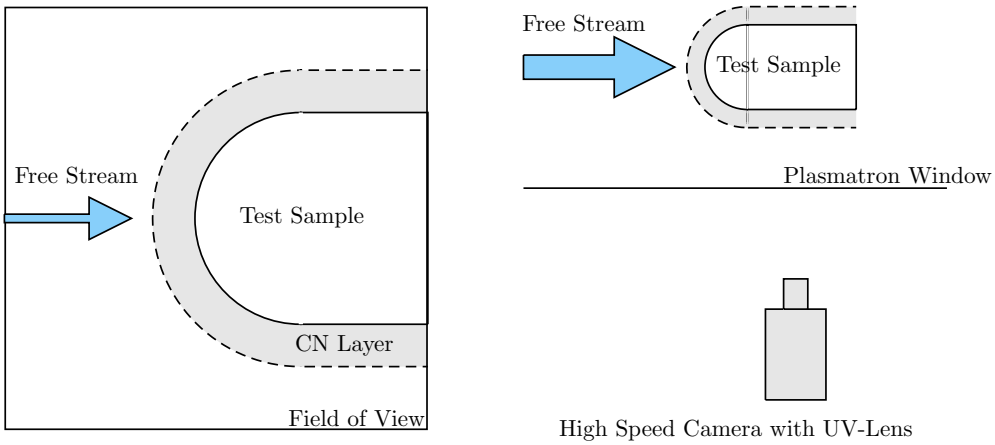

(a) View of camera

(b) Top view

Figure 6.1: Schematic representation of the measurement

Table 6.1: Test Matrix: CN Species

Test	Material	Diameter mm	Filter	Heat Flux MW/m^2	Pressure mbar	acquisition frequency frames/second
1.	Graphite	50	NO	1	200	100
2.	Graphite	50	YES	1	200	100
3.	Cork	50	YES	0.2	200	500

6.2 Test Results

As mentioned in the introduction of this chapter, CN violet is observed in the boundary layer of a graphite sample and a cork test sample. First the graphite sample is tested with and without filter so that the contribution of CN violet to the boundary layer can be invesitgated. Second the graphite is compared to the cork test, both installed with filter, to observe the difference between a pyrolyzing and non-pyrolyzing material.

6.2.1 Graphite Sample: Spatially resolved CN violet emission

The first test performed to study the CN violet in the boundary layer is done with a graphite sample. As already explained this sample contains only carbon (C) and therefore the material will not pyrolyze. When it is subjected to plasma, the material can either chemically react with the oxygen (O_2) or nitrogen(N_2) in the free-stream and boundary layer. The product of the reaction with nitrogen is CN violet.

As shown in table 6.1 two tests are performed with the graphite sample, one with filter and one without. Test 1 is performed without the filter, the original images for this test after being injected for one and ten seconds are shown below, see figures 6.2(a) and 6.3(a), respectively. Similarly figures 6.2(b) and 6.3(b) show the original images for test 2, also after one and ten seconds of injection. The two tests are exactly the same test except that the UV-filter is placed in front of the lens for test 2.

Before the boundary layers of the tests can be compared, there surface and boundary layer edge are detected, using a build-in function of Matlab® , based on a user-given threshold value indicating a percentage of the maximum value in the image. It is aimed to find the contour of the surface edge and the boundary layer edge by setting a threshold on the brightness of the image pixels. An example of the result is shown in figure 6.4. For this image in particular it can be seen that the filter block almost all the light, causing the boundary layer to barely exist.

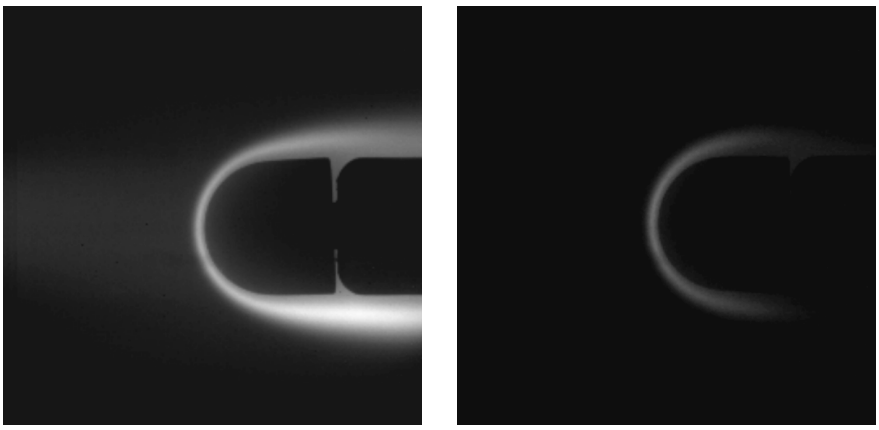

(a) Test 1 (graphite no filter): 1 second after injection

(b) Test 2 (graphite filter): 1 second after injection

Figure 6.2: Original images of graphite samples

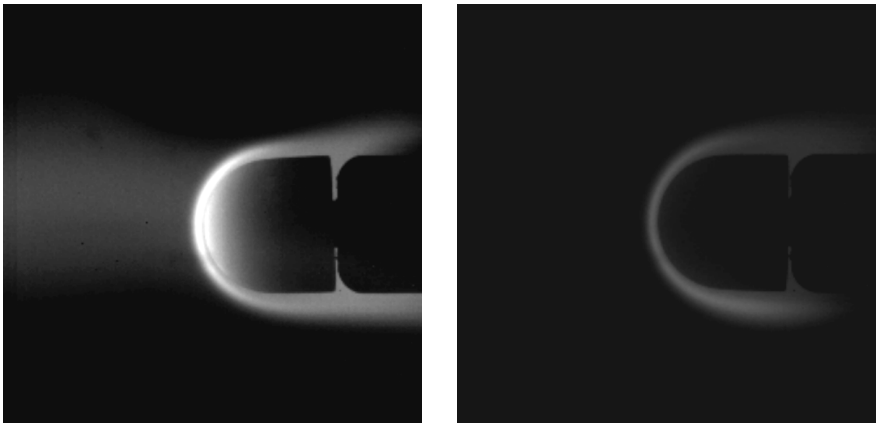

(a) Test 1 (graphite no filter): 10 seconds after injection

(b) Test 2 (graphite filter): 10 seconds after injection

Figure 6.3: Original images of graphite samples

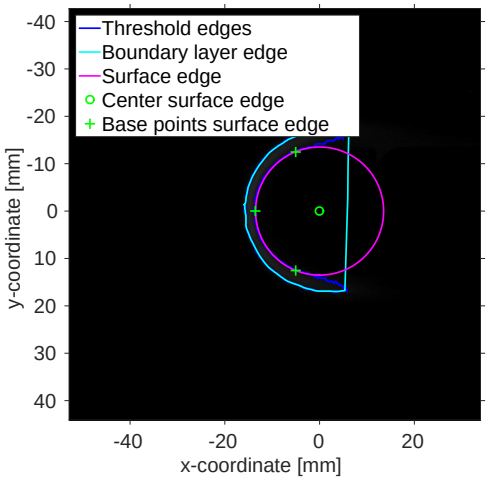

Figure 6.4: Test 2, One second after injection: Graphite sample image with boundary layer and surface edge (With filter)

Look at the two images in figure 6.2. From these images, a clear difference in brightness is apparent. The images of test 2, with filter, are darker than those of test 1, without filter. This is expected, in the test without filter, test 1, there is more light compared to the test with filter, test 2.

To compare the difference of the boundary layer edges between these two tests, the surface edges are scaled so that they match perfectly. By superimposing the boundary layer edges and surface edges unto each other the difference between the boundary layers is assessed. To ensure that no mistakes were made during the superimposing, the surface edges are matched to each other. As both times the test sample was graphite, which does not pyrolyze and only very slowly ablates, the surfaces should still be the same. The result is given in figure 6.5. From this figure it can be seen that the boundary layer of test 2 is smaller in every location, at the stagnation point and at the sides of the surface. This shows that in the beginning of the test the development of CN violet is small compared to the rest of the light in the boundary layer.

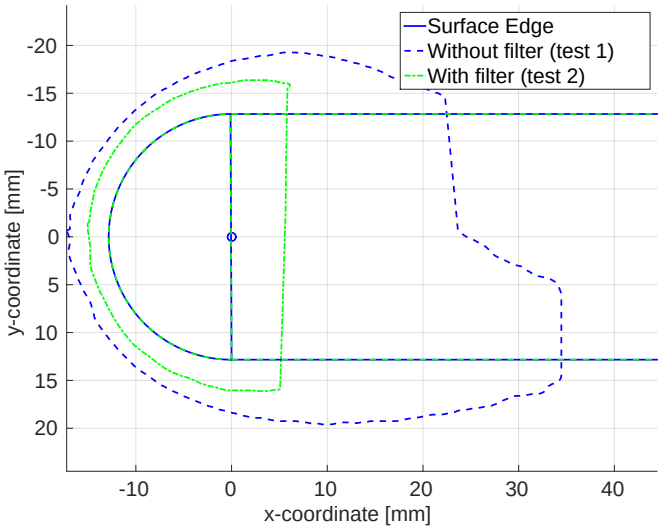

Figure 6.5: Graphite sample comparison of images without (test 1) and with (test 2) filter after one second

To check if this difference is maintained through the entire test, the same figures are produced ten seconds after injection, see figures 6.3. Combining the edges of the two tests and scaling the surface edges figure 6.6 is obtained. From this figure it becomes clear that as the test progresses, the CN violet spreads more into the boundary layer. Also comparing the original figures, figures 6.3, it is clear that still test 1 is the brightest

test. In the figure of test 1 (without filter), figure 6.3(a), it is also clear that the surface has heated up compared to figure 6.2(a). This increase in surface temperature is the mostly likely reason for the increase in CN violet in the boundary layer.

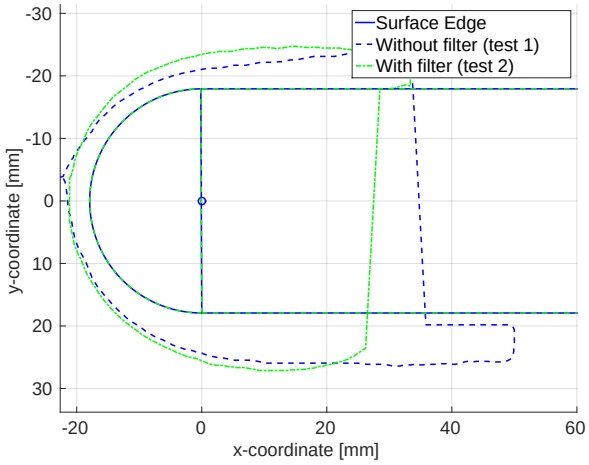

Figure 6.6: Graphite sample comparison of images without (test 1) and with (test 2) filter after ten seconds

A final spatial comparison that is made between these tests, with and without filter, is the intensity across the boundary layer in the Stagnation point, as presented in figures 6.7 and 6.8. Int the figures the vertical black line indicated the location of the surface edge. So the curves on the left side of this line represent the boundary layer in front of the test sample, while on the right side they represent the gases at the side of the sample along the stagnation line. Figure 6.7 shows the gas profile one second after injection. This shows that the brightest part of the boundary layer is located a in front of the surface edge for both tests, with and without filter. Now observing figure 6.8 it is noticed that the peak of the CN violet boundary layer is shifted towards the test sample, while the overall boundary layer profile has not changed significantly. This indicates that as the test progresses and the CN violet production increases with the heating of the test sample, it also moves towards the surface. To investigate if this is a general trend or just an instantaneous effect of the plasma jet fluctuations, the intensity of four points in the boundary layer at three different locations is assessed next.

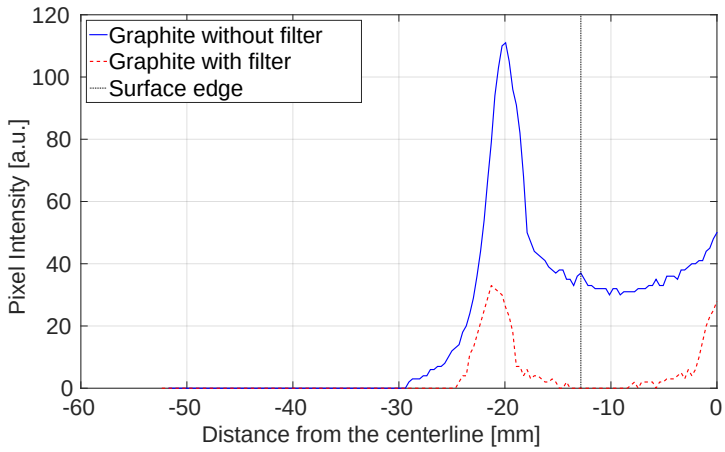

Figure 6.7: Boundary layer profile of test 1 (without filter) and test 2 (with filter) one second after injection. The vertical line represents the surface edge, on the right side of this line the curve represents the intensity of the gases flowing along the surface and the surface intensity

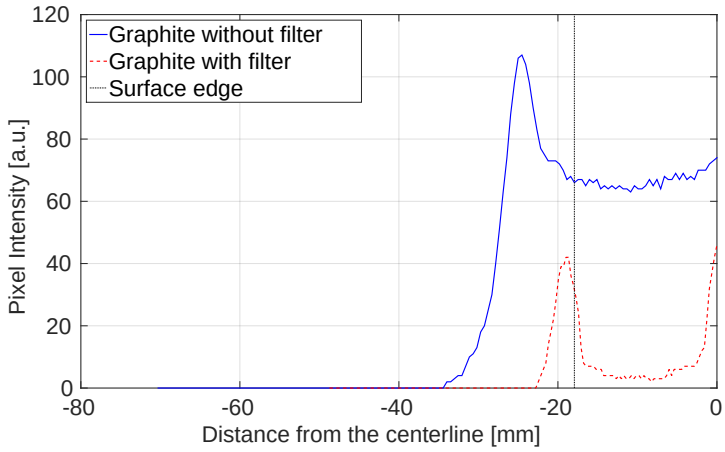

Figure 6.8: Boundary layer profile of test 1 (without filter) and test 2 (with filter) ten seconds after injection. The vertical line represents the surface edge, on the right side of this line the curve represents the intensity of the gases flowing along the surface and the surface intensity

The intensity in four points at three locations is recorded over time and presented in figures 6.9 to 6.12. The first two figures indicate the location of the points and the second two figures display the actual intensity over time given in a percentage with respect to the maximum intensity over the scope of the test in the chosen points. The high speed camera cannot differentiate the wavelengths of the light, it displays the total amount of light per pixel. Off course the camera sensor sensitivity is dependent on the wavelength. After about ten seconds the injection of the sample in the plasma jet is clearly visible, strong rise in the curves.

Now look at figure 6.11 (without filter, test 1) from this the injection of the sample in the flow is clearly visible due to the sudden jump in the intensity after the camera has been recording for about ten seconds. Comparing this initial jump with figure 6.12, which shows the time measurement of the test with filter (test 2), it can be said that the initial jump is not CN violet. From these graphs it becomes clear that CN violet production gradually increases as the intensity of increases over time. As the test progressed, the intensity of the filtered image increases, confirming the initial statement that the CN violet production rises with increasing surface temperature, until it has reached its limit. In the unfiltered image 6.11 there is also a gradual increase in the intensity over time which also reaches a maximum. Notice that the lines for the top point , the line measured 0.5 mm from the top point and the bottom point keep increasing. This is possibly due to the expansion of the test sample, which then crosses the the pixels presented here. So this increase is the heating of the sample surface and not some species in the flow. Finally clearly indicate that the side-wall region and the stagnation point react the same to the plasma jet. The three graphs, both for the test with and without filter, underwent the same changes as test progressed. The only difference between the three locations is that for the unfiltered test, the intensity decreases in the stagnation point with distance to the surface while the intensity is more or less constant at the side-walls. For the filtered image there is a gradient with distance to the surface for all three locations, but the side-wall locations gradient is much different from the stagnation point. In the stagnation point, the intensity is more or less constant for the distances fro the surface, except for 2 mm distance from the surface, which measures barely anything. This indicates that the boundary layer is thinnest in the stagnation point. Also notice that, as indicated in the boundary layer profile comparison, the strongest signal in the stagnation point is measured at 0.5 mm from the surface and not at the surface itself.

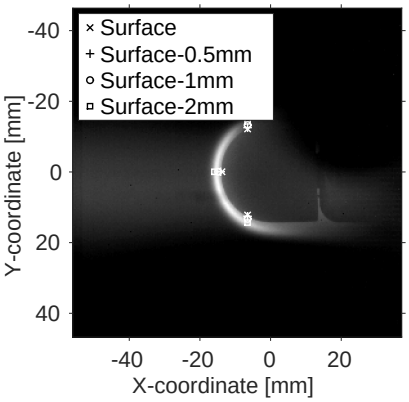

Figure 6.9: Tracking points of test 1 (without)

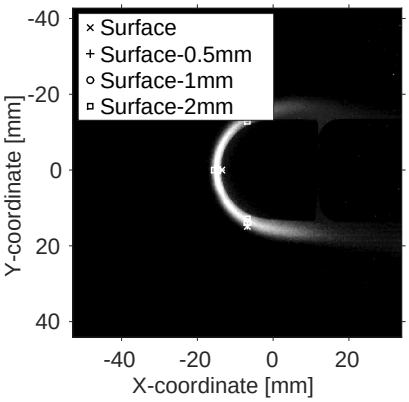

Figure 6.10: Tracking points of test 2 (with)

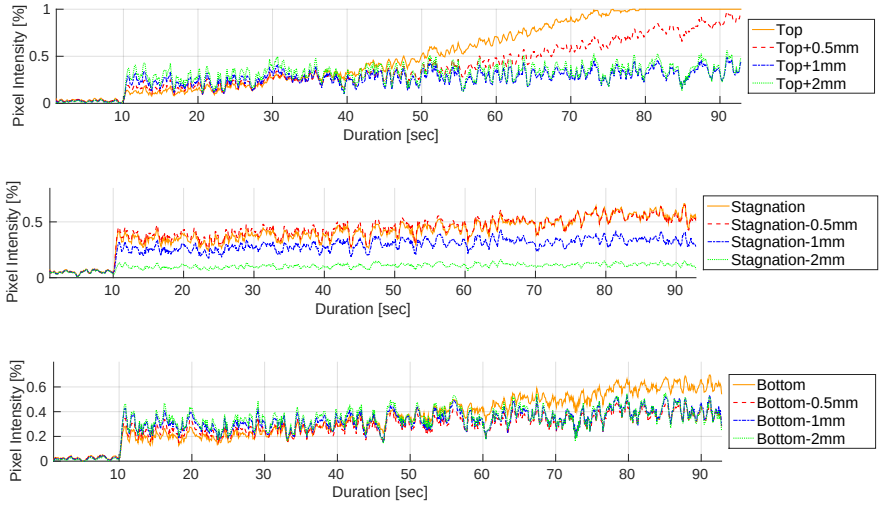

Figure 6.11: Intensity over time in the selected points of test 1 (without filter)

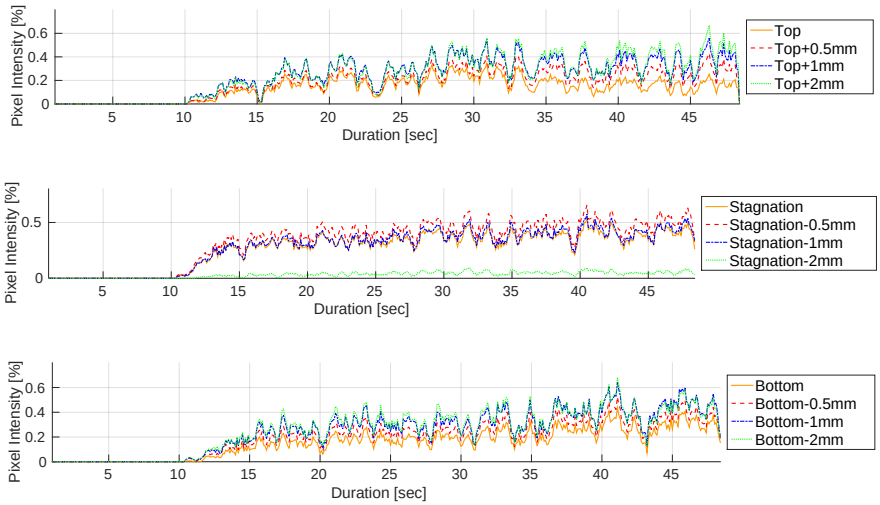

Figure 6.12: Intensity over time in the selected points of test 2(with filter)

From the above assessment of the non-pyrolyzing material (graphite) with and without filter, it can be concluded that the CN violet production begins very gradually as the test sample is injected in the plasma. Also from both the spatial and temporal measurement that was assessed for these two tests production of CN violet and the evolution of the entire boundary layer is independent of the location on the test sample. This is clearly visible in figures 6.5, 6.6, 6.11 and 6.12. In the first two figures (6.5and 6.6), which compares the boundary layer edge shape of the two tests one and ten seconds after injection, it can be seen that the boundary layer edges maintains a constant distance to the surface all around the test sample. Figures 6.11 and 6.12 indicate that the intensity of the boundary layer at the side-wall progresses in the same fashion as at the stagnation point.

6.2.2 Pyrolyzing (Cork) versus Non-Pyrolyzing (Graphite) Material, Both with Filter

As stated before CN violet is a product of both ablation and pyrolysis in pyrolyzing materials. From the above assessment of a non-pyrolyzing material, it has become clear that CN violet knows a gradual production as the material heats up in the flow. Also, there have been no signs that the development of the boundary layer is different for the side-wall or stagnation region. This leads to the conclusion that the pyrolysis plays a major role in the development of the boundary layer. To see if this is in fact true, a similar comparison is made between a pyrolyzing (cork) and non-pyrolyzing (graphite) material. For practicality, the original image is repeated below, see figure 6.13(b). The original image of the cork sample is shown in figure 6.13(a).

The cork sample used in these tests has the same geometry as the graphite sample but the test conditions were different, see table 6.1. In this test the heat flux is reduced to 200 kW/m^2 while the graphite sample is tested at 1 MW/m^2 and the pressure is 15 mbar compared to 200 mbar for graphite. As previously explained, the cork sample contains a lot of phenol and will therefore pyrolyze, while the graphite sample will not. In this thesis pyrolysis is the main process of interest and the speed at which the material pyrolyzes is dependent on the heat flux and pressure. When these are reduced, the consumption of the material will slow down so that the acquisition is easier.

The first thing that is noticed when looking at the original images of the cork and graphite test, see figure 6.13, is that the image of the cork sample is much brighter than the graphite image. The reason for this is that initially there is more CN violet present around the pyrolyzing material, cork, compared to the non-pyrolyzing material, graphite. For a pyrolyzing material the pyrolysis starts very strongly and a large amount of gases is initially released, while for the non-pyrolyzing material the carbon production is mostly dependent on surface temperature, as was explained in the previous section. This leads to the idea that also the boundary layer profile differs between the non-paralyzing and pyrolyzing material.

The boundary layer profile for the cork (test 3) and the graphite material (test 2) are given in figures 6.14 and 6.15. From these images it can be seen that for the pyrolyzing material the boundary layer profile is different from the non-pyrolyzing material. The peak in the curve, representing the intensity of the CN violet emission in the flow, of the pyrolyzing material coincides with the surface edge, which leads to the conclusion that the CN violet production for a pyrolyzing material occurs at the surface. While for the non-pyrolyzing material this is a little in front of the surface edge. As stated above, the peak of the non-pyrolyzing material shifts towards the surface as the test continues. To see if there are also differences in the evolution of the CN violet production of these two materials, the development is discussed next.

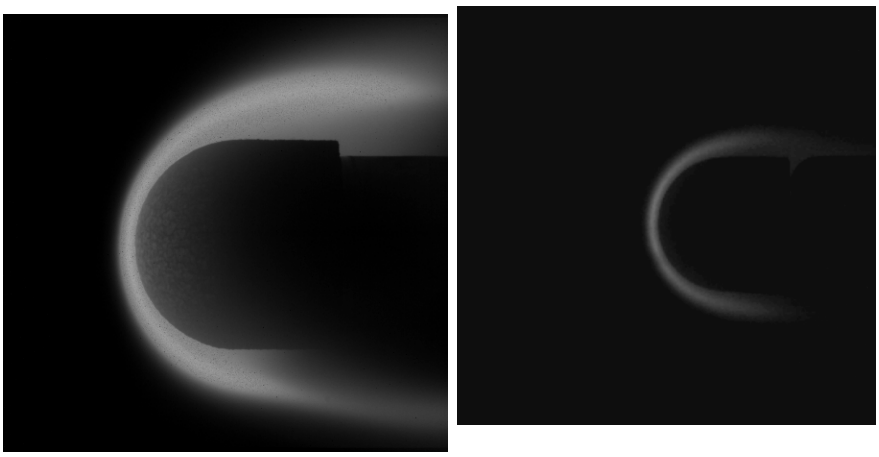

(a) Test 3 (cork sample): 1 second after injection

(b) Test 2 (graphite sample): 1 second after injection

Figure 6.13: Original images of cork and graphite sample, respectively

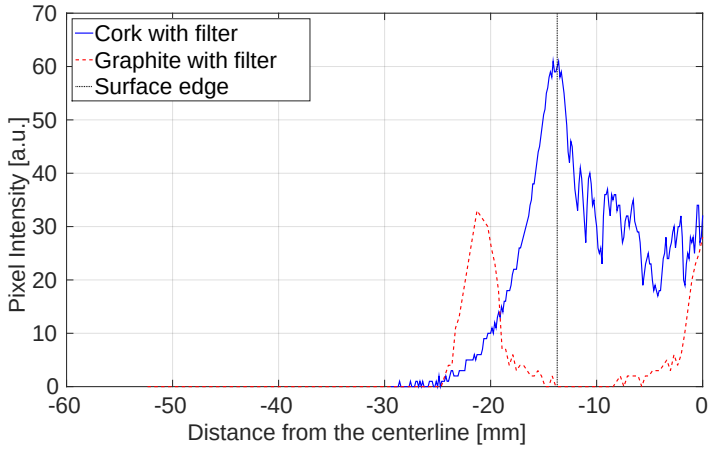

Figure 6.14: Boundary layer profile of test 2 (graphite sample) and test 3 (cork sample) one second after injection. The vertical line represents the surface edge, on the right side of this line the curve represents the intensity of the gases flowing along the surface and the surface intensity

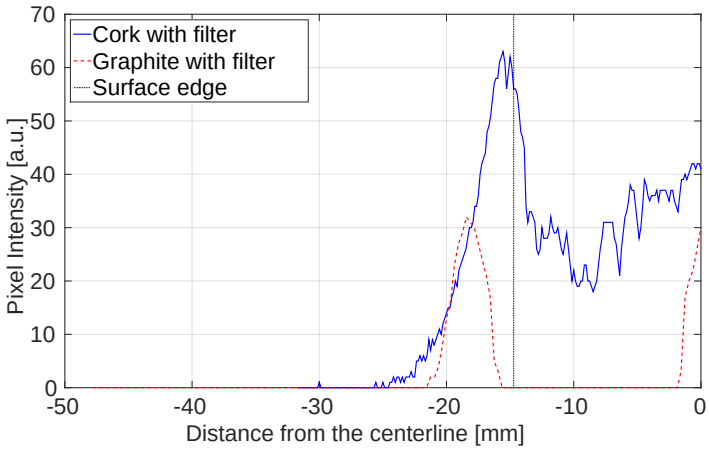

Figure 6.15: Boundary layer profile of test 2 (graphite sample) and test 3 (cork sample) ten seconds after injection. The vertical line represents the surface edge, on the right side of this line the curve represents the intensity of the gases flowing along the surface and the surface intensity

To see how the pyrolysis affects the boundary layer during the entire tests, the boundary layers are plotted with respect to time. In these plots the intensity of four points is presented. This is done in the stagnation point and on both sides of the test samples. The points are presented in figures 6.16 and 6.17 for the cork and graphite sample, respectively. The plots representing the changes that occur in these points over time are given in figures 6.19 and 6.18 for the cork and graphite sample, respectively. To make the comparison between the plots easier, their pixel intensity is scaled with the maximum pixel intensity throughout the entire test in those points.

What stands out is that in the stagnation point of the cork sample, the intensity decreases over time until it reaches zero at the end of the test. This is not a surprise as ablated cork is a porous material and thus part of the gases that develop during pyrolysis are pushed in the sample and will flow out at a different location. Also as previously stated, the strength of the pyrolysis decreases over time, which is the second contributing factor. At the beginning of the test, the material is much denser and therefore not as much of the gases can penetrate the sample and thus the boundary layer is thicker in the beginning of the test. The plots representing the measurements on the sides of the cork sample act completely different. At these locations, it seems that the boundary layer does not change a lot. Because of the instability of the plasma-jet, there are fluctuations in the signal. The graphite sample on the other hand experiences an increase in CN violet as the test progresses until it reaches its maximum, which can be explained by the gradual increase in surface temperature of the material causing carbon to be released. The CN violet levels will stay at there maximum until the end of the tests.

From this is is concluded that pyrolyzing material do not respond as originally assumed in literature and that Weng et al. were right about the importance of the multidimensional aspect of pyrolysis, see section 3.2. The two biggest differences is the presence of pyrolysis gases which initially blow out of the material at high pressure, and the porosity of the left over material after pyrolysis. Figure 6.19 shows that as the pyrolysis gases become weaker over time, the free stream forces some of the pyrolysis gases to flow through the material before they leave the material. In the following chapter it is attempted to visualize this internal flow of pyrolysis gases.

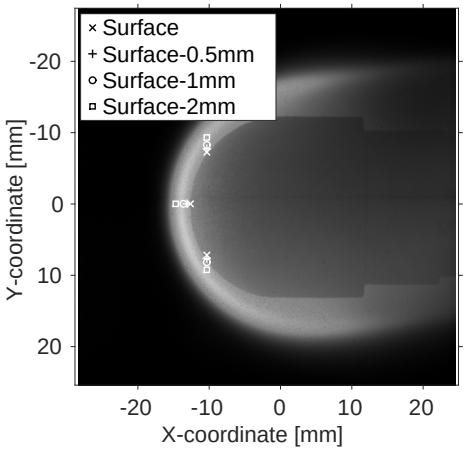

Figure 6.16: Points used the tracking of the cork sample

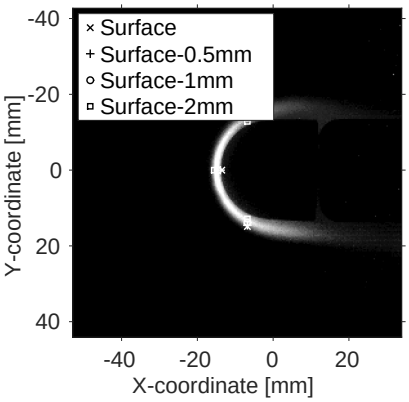

Figure 6.17: Points used for the tracking of the graphite sample

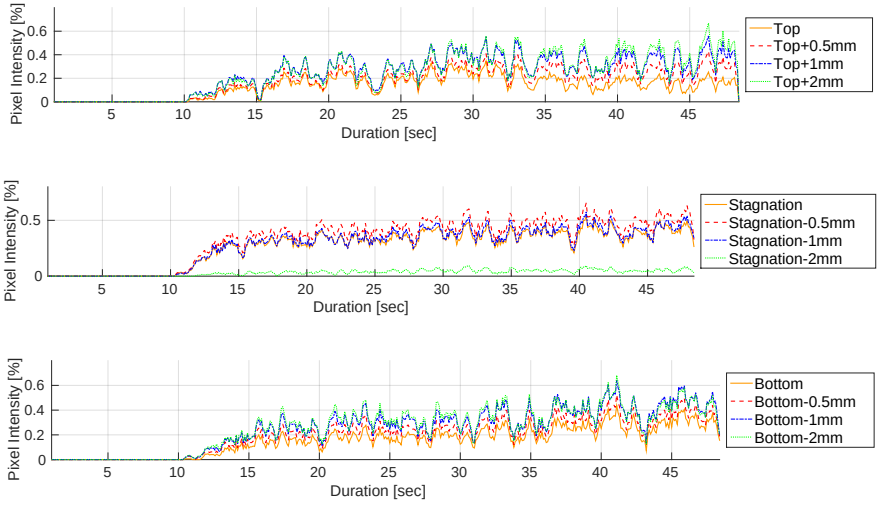

Figure 6.18: Intensity over time in the selected points of test 2 (graphite sample)

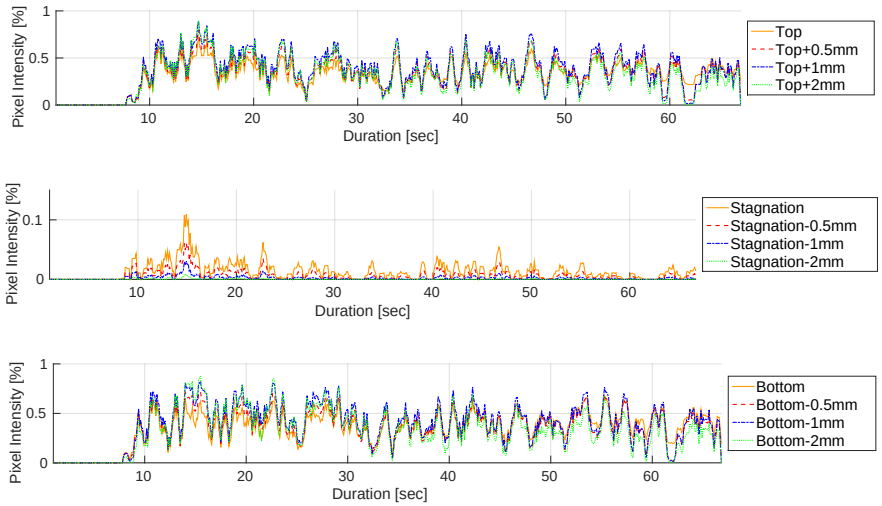

Figure 6.19: Intensity over time in the selected points of test 3 (cork sample)

Chapter 7

Pyrolysis Visualization Technique

As mentioned in the previous section, due to the porosity of the ablation materials their exists a transport of gases through the test sample as it pyrolyzes. This is nothing new, Weng and Martin (2013), but the influence of the material porosity on its performance has remained unknown. In this chapter it is aimed to study the flow of pyrolysis gases in the material, unfortunately there is no measurement technique that is able to visualize this gas flow. Therefore a method is developed based on the seeding technique of Winter et al. (2014). He placed a seeding material inside a test sample, the material he used had similar thermal properties as the carbon and the char that is left behind after pyrolysis. As the surface receded and the seeding material appeared at the surface it too was subjected to the high enthalpy environment and ablated as well, giving insight in the recession velocity of the material. By observing the chemical species in the flow around the test sample he was able to obtain a time resolved recession measurement.

The method here is modified so that it allows the user to track the pyrolysis gases, therefore the seeding material and installation of the seeder material needs to be altered. Winter simply drilled a hole in the material and filled it up again. It is believed that the damage caused by this method can cause a significant change in thermal performance. Also since the aim is to visualize the pyrolysis gases and not solid material, therefore it is key that the seeder undergoes the same process as the resin inside the test sample.

Throughout this testing phase, emission spectroscopy is used, which is shortly explained in section 7.1. In the alteration of Winter's method, first a suitable material is selected in section 7.2. A testbench is set-up to test several materials to investigate their emission response under high temperatures. When suitable materials are identified, the materials are installed in a test sample and tested in the VKI Plasmatron under typical high enthalpy testing conditions, see section 7.3.

7.1 Measurement Technique

The measurement technique to find a feasible seeder material is emission spectroscopy. This technique is used in both steps of finding a suitable visualization technique. In the preliminary testing phase, the biggest advantage of the technique is its wide spectrum range, 200 nm to 1200 nm. This wide range gives the option to test the materials without worrying that their emission signature will not show up in the measurement. The only important factor to keep in mind is to aim the collimated beam to the location where it is expected to measure the materials. For the plasmatron testing it is also chosen to work with this technique since it is easy to step up and does not require a special filter or lens like imaging techniques often do.

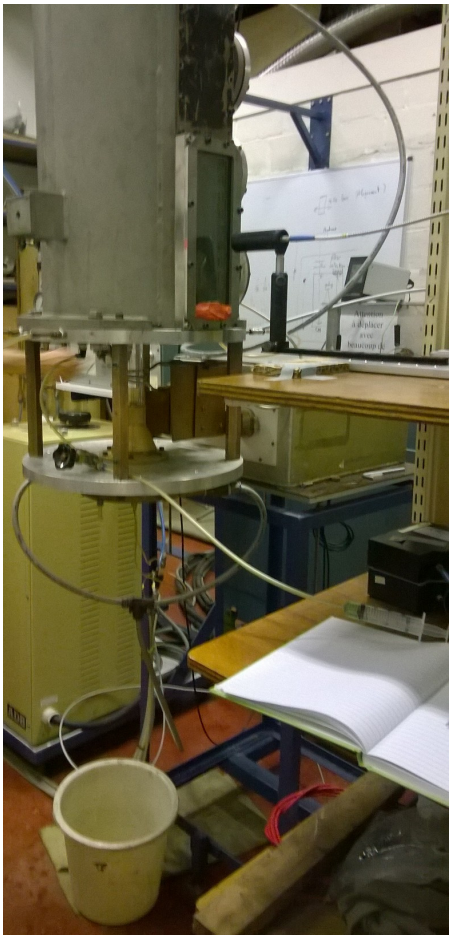

Figure 7.1: Testbench set-up

7.2 Seeder Material Selection Tests

The feasible materials are mainly tested in the testbench to ensure they have a strong emission signature, not every material has the same probability of emitting a strong light signal. This and other criteria for the seeder material are listed below, also a list is given of the selected materials with thermal properties and characteristic wavelengths at which they emit light, see table 7.1. The pressure inside of the test sample at which pyrolysis occurs is unknown, the temperatures in the table are therefore given at atmospheric pressure.

Even though there exist elaborate databases of the emission lines of various materials, it is chosen to test the materials. The databases only give theoretical wavelengths and probabilities of the likeliness that these are in fact the wavelengths at which light is emitted. To be sure that the materials signature is clear and strong the tests were performed and used as a selection procedure.

- **Melting and boiling temperature:** Ideally the tracer material will become gaseous at the exact moment that the resin undergoes this process as well. Unfortunately the temperature at which pyrolysis starts is not exactly known, due to underlying decomposition processes. Therefore the materials cover a range of different melting and boiling temperatures. If it turns out that a high and low temperature material is suited for seeding the material, these can be combined to give a thermal profile of the material, similar to a thermocouple. A thermal profile of an ablation material is presented in section 3.3.
- **Clear emission line signature:** Every chemical element emits light at different wavelength, when a couple of the emission lines from a clear shape in the complete spectrum, for example two close peaks, it makes the element easy to identify from the other molecules and elements in the flow.
- **Easy handling qualities:** In the search for a tracer material also the handling qualities play an important role, this not only influences the testing method in the testbench, but also the method used to implement the tracer into the test sample. When placing the tracers in the test sample it is of vital importance ensure the structural integrity and surface quality of the sample.

Table 7.1: Tracer material Specifications

Material		Thermal properties [°C]		Emission Wavelengths [nm]
Name	Symbol	Melting	Boiling	
Copper	Cu	1084	2575	324, 327
Aluminum	Al	660	2467	309, 396, 1125
Zinc	Zn	419	910	328, 330, 335
Lead	Pb	327	1750	280, 283, 364, 368, 374

7.2.1 Test Progression

In the testbench the materials will be heated such that they start emitting light. This means the the testbench simply needs to be a hot enough source. It is chosen to use a simple gas burner for this. For safety purposes the testbench is installed with a hood, such that the smoke and the fumes created while burning the materials are safely removed. For the first attempt the material was reduced to powder by sanding larger pieces, this powder was then held in the gas burner flame. First some of the powder was simply placed in a spoon which was held in the flame, this did not yield any success. Then a thin wire was dipped in distilled water, to avoid sodium (Na) to corrupt the measurement and then dipped in the powder and again held in the flame. Also this did not give any good results. Because the seeder material was solid, it simply melted and fell of the wire. The drops then fell through the flame before its emission signature was detected. This lead to the conclusion that the seeder material needed to be used in another form instead of solid and that the flame was not hot enough to excite the seeder material so that its emission could be measured.

In the second attempt, the gas burner was replaced by a blow torch in the hope that this could excite the seeder materials. The main difference between a gas burner and a blow torch is that the blowtorch adds oxygen to the gas, which gives a very bright white flame and it a lot hotter than the regular gas burner. As explained above the seeder materials in their solid form did not melt, evaporate and got excited in the short amount of time that they were submerged in the flame. Therefore it was decided to dissolve them into a solution using hydrochloric acid (HCl). When the material are dissolved in HCl they became liquid which removed one of the steps into emitting light. The chemical equations are given in equation 7.1. The hydrogen (H_2) in the equation is gaseous and therefore, it does not influence the original material. Due to dissolving the materials, they combined with chlorine (Cl_x), this combination makes the metals to share one or more electrons with the chlorine and thus the metals become ionized.

Now the heat of the flame is used to vaporise the solution and separate the molecule with chlorine. To take full advantage of the liquid state of the materials, they are sprayed in the flame. By using a spray small droplets are inserted in the flame, these make it easier for the flame to excite the materials. Due to combinations of the metals and the chloride, the boiling point of the material changed, the new values are given in table 7.2.

$$2HCl + Cu \rightarrow CuCl_2 + H_2 \tag{7.1a}$$
$$6HCl + 2Al \rightarrow 2AlCl_3 + 3H_2 \tag{7.1b}$$
$$HCl + Zn \rightarrow ZnCl_2 + H_2 \tag{7.1c}$$
$$2HCl + Pb \rightarrow PbCl_2 + H_2 \tag{7.1d}$$

7.2.2 Test Results

The results of the material response is presented in table 7.2. It should be noted that when lead is dissolved in hydrochloric acid, it creates lead-chloride crystals and therefore the lead is actually not present in the liquid part of the solution. This also means that the lead solution cannot be sprayed into the flame. It is therefore that lead is considered as not feasible and indicated with 'Not available' in the table. Also because the materials are now combined with chlorine, the thermal properties have changed. Now only the boiling point is of interest since the materials are liquid. Also the spectra of the tests are given in figures 7.2 through 7.4, they are zoomed to the region corresponding with the theoretical wavelength from the NIST database. The signature quality of the seeder material is judged based on the figures below. The signature quality is defined as a clear signature, are there some emission lines that lie close together in a distinct group, and is the signal produced by the material strong enough to appear above the noise of the measurement. The emission of the tracer material needs to be clear and strong so that it can stand out from all the other species encountered in the boundary layer, as seen in chapter 5. [National Institute of Standards and Technology]

Figure 7.2 presents the signature of copper as it was sprayed in the blow torch flame. The red dotted lines represent the theoretical signature of the copper, therefore it is expected that the emission lines will show up here. For copper the emission lines are two lines about 3 nm apart which makes the signal very distinct. Second, the signal needs to be strong so that it can stand out from the noise encountered in a test where it would be injected in the test sample. From the results for copper it is concluded that this is a suited material for the visualization of the pyrolysis gases. The signature for aluminum are multiple lines, see table 7.1. From these lines the emission should be strongest at lines 309 and 396 nm. Looking at the test results in figure 7.3 it can be seen that these lines are far apart and thus it would be difficult to know if they are indeed aluminum, also the lower line at 309 nm directly falls into the signature of OH. This combined with the weakness of the signal produced by aluminum makes that it is an unsuited tracer material. Finally zinc was tested, similar to copper zinc has two emission lines that are located closely together as shown in table 7.1. The intensity of the zinc signal is weaker than that of copper, but it is still visible, figure 7.4. Therefore zinc is also qualified as a suited tracer material.

Table 7.2: Solution boiling points and Testbench Results

Material [Symbol]	Boiling Point [°C]	Signature Quality
$CuCl_2$	1490	Good
$AlCl_3$	178	Poor
$ZnCl_2$	756	Good
$PbCl_2$	950	Not available

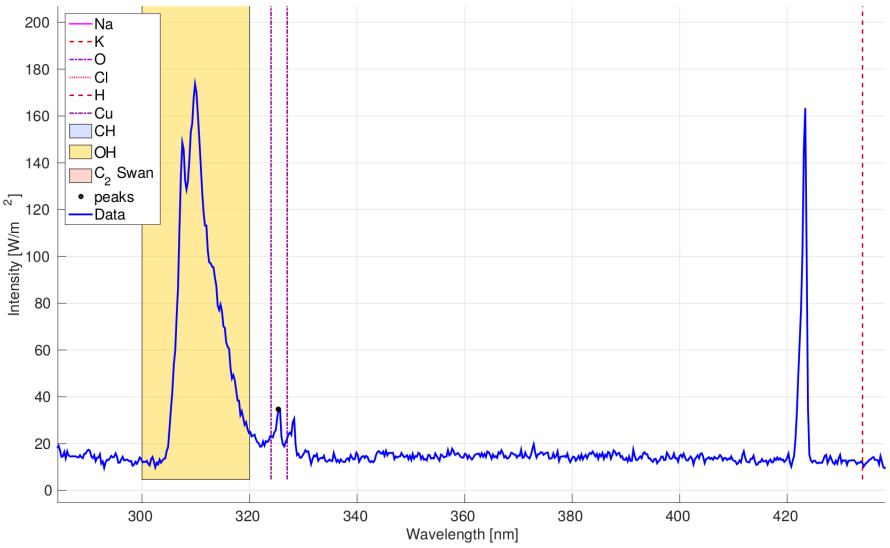

Figure 7.2: Testbench result Cu^{+2} (zoomed in)

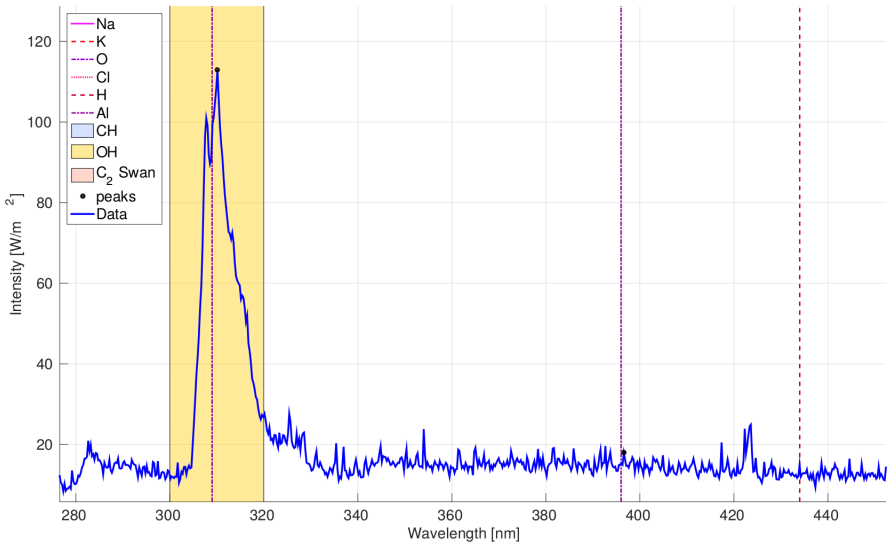

Figure 7.3: Testbench result Al^{+3} (zoomed in)

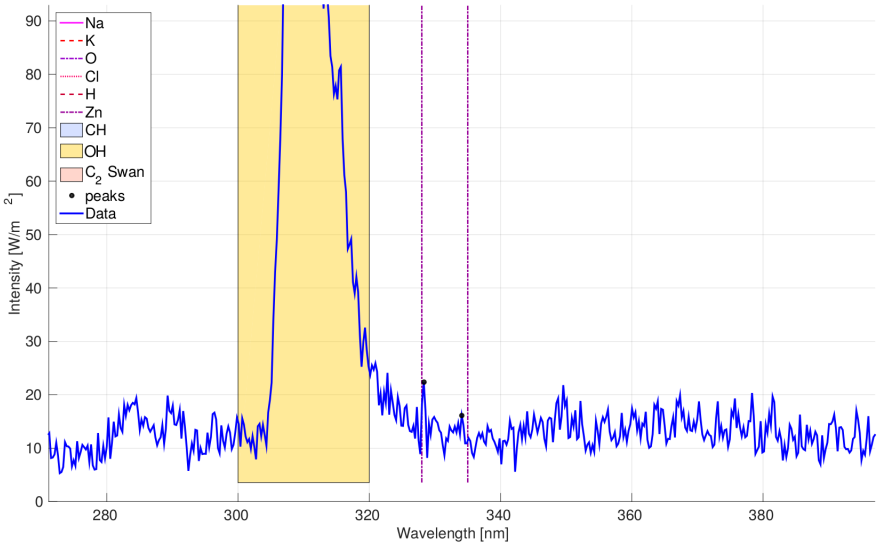

Figure 7.4: Testbench result Zn^{+2} (zoomed in)

7.3 Proof of Concept

In the previous section, different materials were selected and tested to see if their emission response was strong enough that it can stand out from the other chemical species present during thermal protection material testing. In table 7.2 the results of these preliminary tests are given and here it can be seen that only Zinc (Zn) and Copper (Cu) turned out to have a distinct signature. This can also be seen in figures 7.4 and 7.2. The wavelengths at which these two materials emit light is very close to each other, see table 7.1. Because the wavelengths are close to each other the signatures might corrupt the measurements of the other seeder, when they are used together.

In this section, the zinc solution is tested in an actual cork test sample to validate the concept. At this point, the tracer is not yet used to actually obtain information on the pyrolysis gas flow. This validation test is performed to see if the material still shows up with many other species present. Table 7.3 gives the test conditions and acquisition settings for the validation test. The solution was injected in the test sample using a syringe.

From the results of these tests, given in figure 7.5, it is proven that this technique can indeed be used to track the pyrolysis flow in the material. The figures show two moments in time, in the first, figure 7.5(a), the moment just before zinc enters the flow is recorded. Figure 7.5(b) shows the next time step, where zinc is clearly present. The figures are again zoomed in upon the area of interest. In the figures an additional weaker emission line of zinc is observed, indicating that the signal of the emission is strong and making the signature more distinct. From this test it is concluded that it is possible to visualize the pyrolysis gases as they leave the test sample at the side-wall.

Table 7.3: Test Matrix: Plasmatron test with zinc tracer

Test condition & Measurement settings	Zinc cork test
Sample diameter [mm]	50
Heat flux [kW/m^2]	1
Pressure [mbar]	15
Integration time [ms]	200
Acquisition frequency [Hz]	1
Save Every x file	5

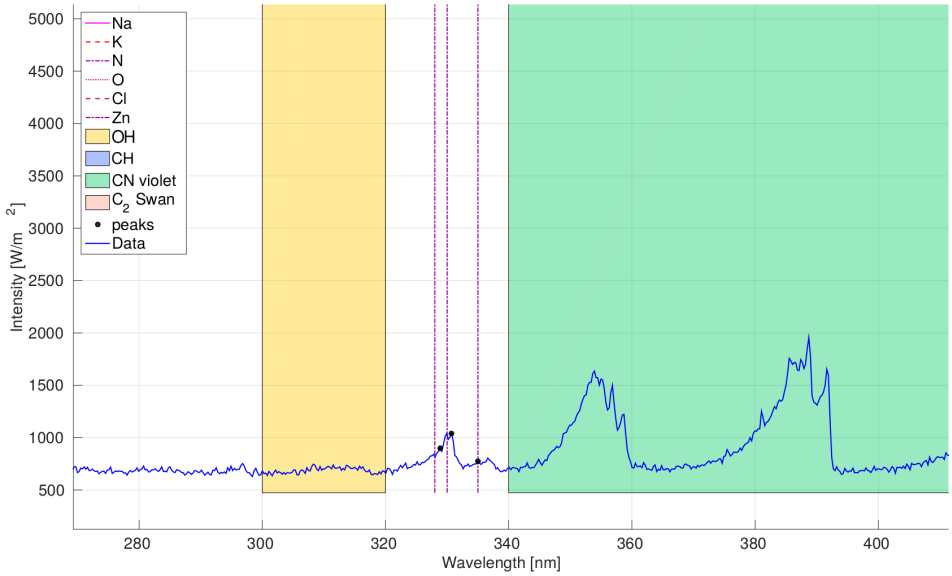

(a) After 1.4 seconds injected in the plasma jet

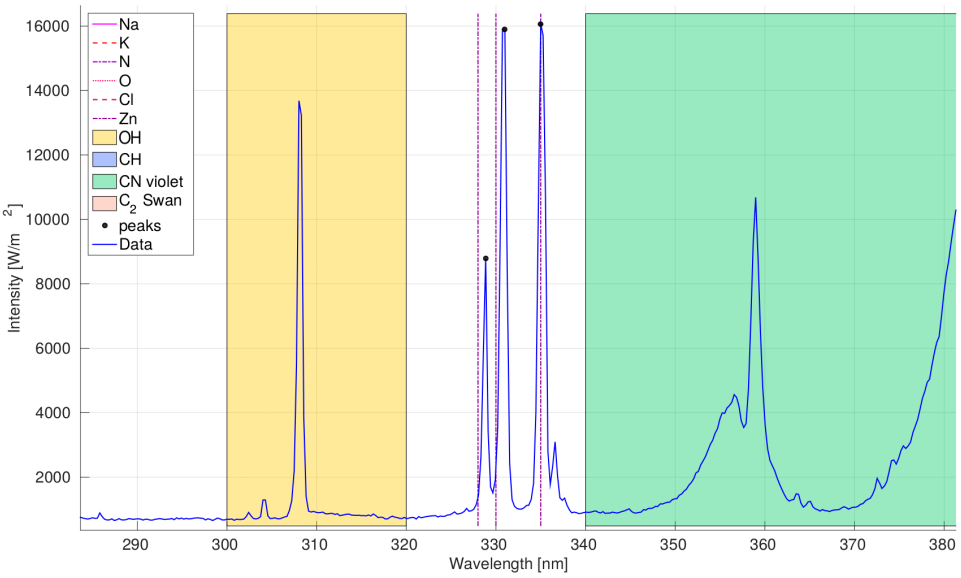

(b) After 1.6 seconds injected in the plasma jet

Figure 7.5: Plasmatron test result at two following time steps and zoomed in on the characteristic wavelengths of zinc

Chapter 8

Conclusion

The goal of this project was to characterize the off-stagnation point pyrolysis process. In order to understand the need for this investigation, first a framework was given of the flight regime, the test facility and measurement techniques, the material, numerical and experimental simulations. This framework offers clear boundaries to which this investigation belongs. To understand the transport phenomena as described by Weng and Martin (2013) and their possible influence on the overall performance of ablative thermal protection materials, three sets of tests have been conducted during this project.

First the chemical and thermal boundary layer outside of the stagnation point was observed, chapter 5. Based on the spatial and temporal measurements made during this test campaign, it can be concluded that the main radiators in the side-wall flow are CN violet and C_2 Swan. Also the intensity of their emission signal decreases with distance to the surface and increases with decreasing sample size.

Next the CN violet contribution was observed more closely in chapter 6, because CN violet is both a pyrolysis as well as an ablation product. During this part of the project, the CN violet was observed for a pyrolyzing and a non-pyrolyzing material. First the non-pyrolyzing material was tested with and without UV-filter to observe the contribution of CN violet in the boundary layer. Second the same assessment was made for a pyrolyzing and non-pyrolyzing material. From this it was concluded that the presence of pyrolysis gases changes the entire reaction of the material to the flow. Due to pyrolysis the generation of CN violet knows a violent start, while this is gradual for the non-pyrolyzing material. Also the porosity of the material left behind by pyrolysis affects the boundary layer profile of the material and causes the side-wall to react different than the stagnation point. Which leads to the conclusion that indeed the three dimensional effects are indeed significant.

Finally, based on a new measurement technique developed by Winter et al. (2014) a visualization technique was explored. The goal of this technique was to obtain a seeder material that could be inserted in a test sample without compromising the structural integrity of the material and the surface quality. This last part of the project proofed promising, it is possible to visualize the pyrolysis gases as they exit the material. Unfortunately due to time constraints it was not possible to actually use the technique in a test.

Chapter 9

Recommendations

In this chapter recommendations are made for future reference. The recommendations are split up per test campaign of the project, first the boundary layer characterization, then the CN violet imaging and finally the pyrolysis visualization technique.

9.1 Boundary Layer Characterization

The tests performed at this stage of the research were part of the study of a PhD student. This limited the freedom of the testing, if the tests were to be repeated, the test conditions could be adjusted a little to the need of this investigation.

Also the accuracy of the test set-up was not ideal, because of the simultaneous measurements as part of the PhD research, the set-up used in for this investigation was forced to work around the other set-up. This made that the set-up became large and ended up partially obscuring the walking route in the laboratory, which allowed some miss alignments to enter the system and the aligning of the set-up to be repeated for every test. Due to this re-alignment the distances between the surface and the spectrometer focal points changed from day to day.

9.2 Imaging of CN violet in the Boundary Layer

The imaging of the CN violet emission in the boundary layer was not calibrated for the sensor response to the observed light. This prevented a discussion on the differences between the intensities for the two comparisons. Also even though the filter is supposed to be a 100 % transparent in its operation wavelengths this should be tested to confirm the specifications given by the manufacturers.

An Abel inversion allows a three dimensional response to be determined based on a two dimensional image and the assumption that the test sample and boundary layer are axis-symmetric. As the camera observes all the light along its line of sight, there is more light accumulated in the images than that there actually is in three-dimensional equivalent.

9.3 Pyrolysis Visualization Technique

The technique has been developed based on a time resolved recession tracking technique developed by Winter Winter et al. (2014).

For the validation of the technique the solution was injected using a syringe. This proved to be more difficult to penetrate the material than initially thought, due to the compact nature of the cork material. Also because of this reason it was chosen to inject the solution through the front in stead of the back, causing the surface to be compromised. Also because this method is done by hand, human error is bound to happen and the accuracy of injecting the solution at the right location is small. So for future purposes, a new and more reliable injection method should be employed.

For the actual testing of the pyrolysis gas flow it is more interesting to use an imaging technique that allows the observation of the entire test sample. This will then give a more accurate idea of the gas flow than when an estimation of the outflow region is made. For the imaging technique a light filter should be selected so that only the light produced by the tracer particles can be observed. If the tracer characteristic wavelengths are in the UV-light spectrum then care must be taken to ensure that the lens in front of the camera is not opaque in this wavelength range.

As the characteristic wavelengths of both materials are close to each other, it might be interesting to seek out another material with a different characteristic wavelength. When the wavelengths of two materials are not influencing each other the materials can be injected in the sample at the same time, which gives a time resolved measurement of the flow inside the test sample, given that the materials have a different boiling

temperature. Also as the materials are liquid they do not need to be injected separately, but the solutions can simply be mixed into one solution.

Bibliography

I. Cozmuta and M. J. Wright A. Martin, I. D. Boyd. Chemistry model for ablating carbon-phenolic material during atmospheric re-entry, 2010.

J. C. Adams. Atmospheric re-entry vehicle mechanics.

Amorim. Reinventing thermal protection is aerospace applications, 2013. URL www.amorimcorkcomposites.com.

John D. Jr. Anderson. *Hypersonic and High-Temperature Gas Dynamics*. American Institute of Aeronautics and Astronautics, Virginia, USA, second edition, 2006.

O. L. Anderson. An experimental method for measuring the flow properties of air under equilibrium and non-equilibrium flow conditions, 1964.

N. Bohr. On the constitution of atoms and molecules, 1913.

B. Bottin, O. Chazot, V. Carbonaro, and S. Paris Van Der Haegen. The vki plasmatron characteristics and performance. 1999.

Jean-Marc Bouilly, Francine Bonnefond, Ludovic Dariol, Pierre Jullien, and Frdric Leleu. Ablative thermal protection systems for entry in mars atmosphere. a presentation of materials solutions and testing capabilities. *4th International Planetary Prode Workshop*, 2006.

Jos A. C. Broekaert. *Analytic Atomic Spectroscopy with Flames and Plasmas*. WILEY-VCH Verlag GmbH & Co. KGaA Weinheim, Hamburg, Germany, second completely revised and extended edition, 2005.

M.A. Covington, J.M. Heinemann, H.E. Goldstein, Y. K. Chen, I. Terrazas-Salinas, J.A. Balboni, J Olejniczak, and E.R. Martinez. Performance of a low density ablative heat shield material. *Journal of Spacecraft and Rockets*, 45(2), 2008. doi: 10.2514/1.12403.

S. G. Penoncello and D. G. Friend E. W. Lemmon, R. T. Jacobsen. Thermodynamic properties of air and mixtures of nitrogen, argon and oxygen from 60 to 2000k at pressures to 2000 mpa. *Journal of Physics and Chemistry*, 2000.

T. H. Squire F. S. Milos, Y. K. Chen and. Analysis of galileo probe heatshield ablation and temperature data. 1999.

R. G. Finke. Entry velocities at mars and earth for short transit times, 1993.

R. H. Goddard. Report concerning future developments, 1920.

Bernd Helber, Thierry E. Magin, and Annick Hubin. Material response characterization of low density carbon-phenolic ablators in +high-enthalpy plasma flows.

Bernd Helber, Cem O. Asma, Yacine Babou, Annick Hubin, Olivier Chazot, and Thierry E. Magin. Material response characterization of a low-density carbon composite ablator in high-enthalpy plasma flows. *Journal of Materials Science*, 49(13): 4530–4543, 2014.

I. Cozmuta and N. N. Mansour J. Lachaud, T.E. Magin, 2011.

B. Laub and E. Venkatapathy. Thermal protection system technology and facility needs for demanding future planetary mission. *International Workshop on Planetary Probe Amtospheric Entry and Descent Trajectory Analysis and Science*, 2003.

F. S. Milos and Y. K. Chen. Two-dimensional ablation, thermal response, and sizing program for pyrolyzing ablators. *Journal of Spacecraft and Rockets*, 46(6):1089–1099, 2009. ISSN 0022-4650 1533-6794. doi: 10.2514/1.36575.

NASA Mars Exploration Program & Missions. Mars exploration program & missions. URL http://mars.nasa.gov/programmissions/missions/missiontypes/samplereturns/.

National Institute of Standards and Technology. Nist atomic spectra database lines from. URL http://physics.nist.gov/PhysRefData/ASD/lines_form.html.

Newport Corporation, 2015. URL http://www.newport.com/.

Ocean Optics. Hr4000 and hr4000cg-uv-nir series high-resolution fiber optic spectrometers. Dunedin (Florida), USA, 2001-2008.

Francesco Panerai. *Aerotermochemistry Characterization of Thermal Protection Systems*. Thesis, 2012.

Francesco Panerai and Olivier Chazot. Characterization of gas/surface interactions for ceramic matrix composites in high enthalpy, low pressure air flow. *Materials Chemistry and Physics*, 134(2-3):597–607, 2012. ISSN 02540584. doi: 10.1016/j.matchemphys.2012.03.036.

R. W. B. Pearse and A.G. Gaydon. *The Indentification of Molecular Spectra*. Chapman & Hall LTD, London, third edition edition, 1963.

M. Rydkin. High-frequency induction plasmatron, 2012.

L. M. Gilbert S. M. Scala. Sublimation of graphite at hypersonic speeds. *AIAA Journal*, 1965.

Isil Sakraker and Cem Ozan Asma. Experimental investigation of passive/active oxidation behavior of sic based ceramic thermal protection materials exposed to high enthalpy plasma. *Journal of the European Ceramic Society*, 33(2):351–359, 2013.

Semrock. URL \http://www.semrock.com.

J. Lachaud and D. Bianchi T. van Eekelen, A. Martin. Numerical simulation of ablative-materia response: Code and model comparisons. 2004.

ThorLabs Inc. URL \https://www.thorlabs.com/index.cfm.

W.P. Meyers J.M. Uhl, J. Owens and D.G. Fletcher. Pyrolysis simulation in an icp torch facility. (AIAA 2011-3618), 2010.

von Kármán Institute for Fluid Dynamics. von kármán institute for fluid dynamics. URL https://www.vki.ac.be/index.php/home-v16.

W. G. Vincenti and C. H. Kruger, Jr. Introduction to physical gas dynamics (reprint), 1917.

Haoyue Weng and Alexandre Martin. Multi-dimensional modeling of charring ablators. 2013. doi: 10.2514/6.2013-2635.

Michael Winter, Mairead Stackpoole, Anuscheh Nawaz, Gregory L. Gonzales, and Thanh S. Ho. Remote recession sensing of ablative heat shield materials. 2014. doi: 10.2514/6.2014-1151.

E.V. Zoby and E.M. Sullivan. *Effects of Corner Radius on Stagnation-Point Velocity Gradients on Blunt Axisymmetric Bodies*. Langley Research Center, Hampton, Va, 1966.

Appendix A

Complete Test Matrix

Table A.1: Test Matrix: Boundary layer characterization (part 1)

Test number	Date	Sample diameter mm	Heat Flux MW/m^2	Pressure mbar	Duration sec
23	26/09/14	15	0.46	41	82
15	06/10/14	15	1.00	15	37
18	07/10/14	15	3.00	15	17
21	07/10/14	15	0.28	41	170
25	08/10/14	15	1.00	200	37
26	09/10/14	15	3.00	200	13
16	09/10/14	11	1.00	15.50	34
22	10/10/14	11	0.28	41	120
27	10/10/14	11	0.46	61.80	
3 repetition	19/11/14	15	0.46	61.80	65
18 repetition	20/11/14	15	3.00	15	13
9 repetition	03/12/14	25	0.46	61	100
14 repetition	04/12/14	25	1.00	15	48

Table A.2: Test Matrix: Boundary layer characterization (part 2)

	Integration Time			Acquisition freq.	Saving freq.
	M14	C19	F71		
	ms	ms	ms	Hz	Every xth file
23	50	50	100		1/5
15	100	100	100	5	5
18	20	20	10	5	5
21	150	150	75	5	5
25	100	100	50	5	5
26	20	20	10	5	2
16	N/A	N/A	N/A	N/A	N/A
22	200	200	200	1	1
27	200	200	200	1	1
	M19	C71	F14		
3 repetition	300	300	300	1	0.5
18 repetition	20	10	20		
9 repetition	200	200	200	2	1
14 repetition	100	50	100	2	2